SAPIENZA
Università di Roma
Facoltà di Scienze Matematiche Fisiche e Naturali

DOTTORATO DI RICERCA
IN GENETICA E BIOLOGIA MOLECOLARE

XXXV Ciclo
(A.A. 2022/2023)

Live-cell imaging of non-coding RNAs dynamics in ALS condensates

Dottorando
Erika Vitiello

Docente guida
Prof. Irene Bozzoni

Tutore
Dr. Davide Mariani

Coordinatore
Prof. Fulvio Cruciani

Index

1. GLOSSARY

- **ALS** Amyotrophic Lateral Sclerosis
- **BFP** Blue Fluorescent Protein
- **BSJ** Back-Splicing Junction
- **circRNAs** circular RNAs
- **DCP1A** Decapping mRNA 1A
- **Dlc1** Deleted in liver cancer-1
- **FAs** FUS Aggregates
- **FISH** Fluorescence *in situ* hybridization
- **FP** Fluorescent Protein
- **fRNAs** fluorescent RNAs
- **FTD** Frontotemporal Dementia
- **FUS** Fused in Sarcoma
- **FUSmut** FUS protein carrying the pathological P525L mutation
- **G3BP1** Stress Granule Assembly Factor 1
- **GFP** Green Fluorescent Protein
- **Hdgfrp3** Hepatoma-Derived Growth Factor-Related Protein 3
- **ICSs** Intronic Complementary Sequences
- **IDRs** Intrinsically Disordered Regions
- **LLPS** Liquid-liquid Phase Separation
- **lncRNAs** Long non-coding RNAs
- **miRNAs** microRNAs
- **MNs** Motor Neurons
- **mRNA** messenger RNA
- **$NaAsO_2$** Sodium Arsenite
- **ncRNAs** non-coding RNAs
- **NLS** Nuclear Localization Signal
- **PBs** Processing Bodies
- **pre-mRNA** precursor mRNA
- **PrLD** Prion Like Domain
- **qPCR** quantitative PCR
- **RNAi** RNA interference
- **RNP** ribonucleoprotein
- **ROIs** Regions Of Interest
- **SGs** Stress Granules
- **SIM** Structured Illumination Microscopy
- **smFISH** single-molecule FISH
- **WT** wild-type

2. SUMMARY

In the last few years, interest around non-coding RNAs (ncRNAs) has been growing as they have been found to be involved in several physiological and pathological processes. In fact, their expression is highly enriched in neuronal tissues and, thanks to their complex and modular secondary structure, they can work as scaffold for other RNAs and proteins for the assembly of ribonucleoparticles (RNPs). These supramolecular structures are known to participate in axonal trafficking, a process usually impaired in neurodegenerative diseases such as Amyotrophic Lateral Sclerosis and in particular in the presence of mutations of several RNA binding proteins, among which FUS. In this context, it is crucial to investigate ncRNA dynamics and kinetics in live cells, in order to unveil novel mechanisms for the understanding of neurodegeneration.

For this purpose, we managed to engineer the motor neuron-enriched circRNA circ-Hdgfrp3 and the lncRNA HOTAIRM1 with an array of Pepper, a novel fluorescent aptamer that shows enhanced stability and brightness if compared with previously described fluorescent RNAs, allowing robust RNA imaging with minimal target perturbation [1].

Combining widefield and structured illumination microscopy, we were able to confirm in live mammalian cells that circ-Hdgfrp3 is loaded in G3BP1 and FUSmut RNPs, possibly determining the mechanism through which it is recruited in pathological aggregates in motor neurons [2]. Moreover, we also observed its interaction with DCP1A-tagged processing bodies, raising promising insight about its function and metabolism.

Notably, we also determined HOTAIRM1 constitutive participation in stress granules, while we observed its involvement in the dynamics of FUSmut aggregation. Moreover, we were able to follow its behavior throughout the induction of oxidative stress, an event that leads to the production of aggregates containing several RNA binding proteins, including FUSmut [3]. Via live imaging assays, we determined that its recruitment in stress granules is not

mediated neither by G3BP1 nor by FUS, consistent with the observation that it does not interfere with stress granules assembly and that it preferentially joins the outer layers of such structures.
Overall, as fluorescent RNA technologies are rapidly spreading and are improved for live-imaging applications, our work provides a novel approach for the investigation of ncRNAs' implication in neurodegenerative diseases with a super-resolution potential in live neuronal cells.

3. INTRODUCTION

3.1 Non-coding RNA revolution

In the early 2000s, the spread of next-generation deep sequencing allowed the analysis of the human genome in its whole complexity. The International Human Genome Sequencing Consortium first, and the Encode Project Consortium later, revealed that most of the human genome produces non-coding RNAs and that, on the other hand, only 2% of the whole human genome consists of protein-coding regions. Thanks to their incredible heterogeneity in length, localisation, biogenesis and structure, non-coding RNAs (ncRNAs) were found to have several roles in the regulation of gene expression and in the remodelling of the eukaryotic genome, legitimizing *Homo sapiens* complexity if compared with other sequenced species [4] [5].

The class of non-coding RNAs includes a variety of different species, from short and abundant molecules to long and highly structured sequences. In the first place, biochemical fractionation assays allowed the discovery and functional description of several new species of small nucleolar housekeeping RNAs, added to the already known tRNAs and rRNAs [6].
Worth mentioning, regulatory non-coding RNAs also came into play when Fire and Mello [7] discovered the phenomenon of RNA interference (RNAi) in worms, a mechanism that causes silencing of gene expression after introduction of sense-antisense RNA pairs [8] [9] [10].
RNAi discovery led then to the revival of miRNAs, whose first evidence already appeared in 1993 [11]. miRNAs differ from siRNAs as they act with incomplete base pairing at the 3' UTRs of target mRNAs, driving their translational repression or accelerating their degradation [12] or, alternatively, inducing gene silencing through the deposition of repressive histone marks [13].

Long non-coding RNAs

Long non-coding RNAs (lncRNAs) are commonly defined as RNA molecules longer than 200 nt that lack a long open reading frame and/or do not show codon conservation, hence they do not encode for mRNA, rRNA or tRNA [6]. They can arise from intronic or intergenic regions, or they can be expressed as antisense of protein-coding genes. These RNA molecules show a wide range of evolutionary conservation: some of them are ultraconserved, while others are primate-specific or lack primary sequence conservation. Nonetheless, it is established that lncRNA functions are often related to structural conservation, rather than to primary sequence alignment over species [14].
LncRNAs are characterized by a finely regulated tissue-specific expression, with a consistent enrichment in the nervous system, resulting relevant for many cell biological processes, including differentiation and development [6].
The first important evidence of lncRNA functional roles were provided in the early '90s, thanks to the characterization of H19 and Xist, both acting on chromatin remodelling and architecture [15] [16]. In the following years, many other functions were identified, including scaffolding of protein complexes to genomic loci for transcription regulation [17] [18], regulation of pre-mRNA splicing [19], [20] and post-transcriptional regulation on stability, decay and translation of mRNAs (fig. 2, [21] [22] [23]).
Notably, lncRNAs participate also in many steps of neuronal differentiation and neuron specification, contributing to cell fate determination and to synaptic plasticity [24] [25] [26] [27], [28] [29] and some of them have been correlated to neurodegenerative phenotypes. For example, the isoform NEAT1_2 of the lncRNA NEAT1 is upregulated during the onset of amyotrophic lateral sclerosis (ALS) and is found in nuclear paraspeckles of patients [30], while also in Huntington disease and in frontotemporal dementia an increase of NEAT1_2 pushes signalling pathways specific of neurodegenerative disorders [31]. Another important example is

provided by the non-coding antisense transcript for beta-secretase-1 (lncRNA BACE1AS), which promotes the stability of the (sense) BACE1 mRNA, favouring the formation of amyloid plaques in Alzheimer disease [32].

circRNAs

Almost 25 years ago the class of circular RNAs (circRNAs) was discovered by the Sanger laboratory while studying the functions of viroids as plant pathogens. Electron microscopy allowed the researchers to reveal that these viroids showed a circular structure and failed to be degraded by snake venom phosphodiesterase as well as to be labelled at their 5' and 3' ends [33]. The closed conformation and the absence of a poly-adenylated tail, hampered their detection by standard next-generation RNA sequencing and for many years they were considered an aberrant by-products of splicing events with no functional potential [34]. Indeed, circRNAs can be generated by a non-canonical splicing reaction, the "back-splicing", from a precursor mRNA (pre-mRNA) [35]. In this mechanism a downstream splice donor is joined with an upstream splice acceptor by a 3'-5' phosphodiester bond (fig. 1, [36]) forming the so-called "back-splicing junction" (BSJ).
The back-splicing process is catalysed by the canonical spliceosome machinery and can be enhanced by specific RNA binding proteins, such as Muscle blind (MBL), Quaking (QKI), Fused in Sarcoma (FUS) and SR proteins [37] [38] [39] [40] [41]. These proteins are usually prone to bind matching intronic complementary sequences (ICSs), mostly represented by ALU elements [42] [43], located upstream and downstream the exons involved in the circularisation [44].
Nowadays, the detection of circRNA via Next Generation Sequencing (NGS) is enhanced by non-selecting for polyadenylated transcripts and by treating the samples with RNase R, a 3'-5' exoribonuclease that preferentially digests linear RNAs, thus

enriching the samples for circular molecules [42] [45]. Moreover, NGS can be combined with several available bioinformatics analysis pipelines for the identification of circRNAs from RNA-seq datasets (CIRCexplorer [46]; circBase [47]; circRNA_finder [48]; CIRI2 [49]). Those pipelines aim at detecting "hybrid" reads, matching on the back-splicing junction, the one sequence that univocally identifies circRNAs.

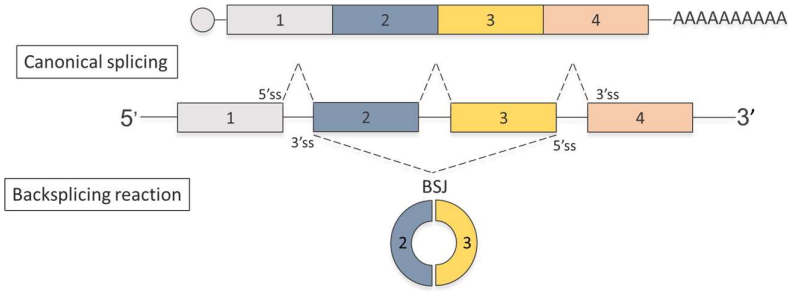

Figure 1: Back-splicing vs. canonical linear splicing.

The pre-mRNA can undergo canonical splicing, that will generate linear mature mRNA (top) or lower efficiency back-splicing, which will generate a circular RNA molecule (bottom). In back-splicing, the downstream 5' splice site donor attacks an upstream 3' splice acceptor. ss, splice site; BSJ, back-splicing junction.

Up to now, the function of few circRNAs has been characterised, even though several studies suggest that they might play important roles in physiological and pathological processes [44].
Indeed, circRNAs expression has reached high levels of complexity during evolution: in fact, one gene locus can give rise to multiple circRNAs through alternative back-splicing within multiple exons or through the selection of alternative donor/acceptor splice sites [50]. Moreover, even though they are generally expressed at lower levels with respect to their linear counterparts [51], their expression can be independent from the linear and even higher, especially in brain tissues and during specific developmental stages of neurogenesis [36] [52] [53] [54]. Besides, because they are resistant to degradation by most of RNA decay machineries, they usually

accumulate post-transcriptionally and their median half-life is longer than the one of the linear transcripts [55]. No common degradation mechanism has been found for circRNAs yet, but it has been shown that the most studied circRNA, CDR1as, undergoes Ago2-mediated cleavage through the interaction with miR-671 [56]. It was demonstrated that CDR1as has multiple binding sites for the miRNA miR-7 and works as decoy against it, thus providing an example of competing endogenous RNA in mammalian brain (fig. 2F, [57]).
Among the other functions that have been attributed to circRNAs, it was shown that the exons that are involved in the circularisation are less present in the linear mRNA, suggesting that circRNAs can affect splicing of their precursors (fig. 2A, [58]). Splicing and transcription regulation seems to be a characterizing trait of nuclear retained circRNAs (specifically ciRNAs, deriving from processed introns lariats and ElciRNAs, back-splicing products with retained introns) (fig. 2A, [59] [60] [61]). Moreover, circRNAs may act as a decoy not only for miRNAs, but also for proteins, as in the case of circMbl (fig. 2E, [37]). Finally, it has been proposed that circRNAs can hold coding capacity and can be translated in a cap-independent manner, allowing the binding of ribosomes through IRES like sequences. For example, Legnini et al. demonstrated that Circ-ZNF609 is associated with heavy polysomes, and it is translated into a protein in a splicing-dependent and cap-independent manner, providing an example of a protein-coding circRNA (fig. 2C, [62]). In this regard, it has also been demonstrated that circRNAs contain extensive m6A modifications; notably, this latter was shown to promote cap-independent circRNA translation through the involvement of the reader protein YTHDF3 and the IRES-specialized translation initiation factor eIF4G2 [63].

Worth mentioning, many circRNAs are produced from neural-specific genes [37] and, even though they show a heterogeneous localisation in neural cells from the soma to the neurites, many circRNAs are enriched in synaptic fractions and synaptosomes,

while their linear counterparts often remain retained in the cell body [52] [36]. Interestingly, expression analysis in developing cultured hippocampal neurons, revealed an increase of circular transcripts corresponding to the time window of synapses formation [36].
Altogether, these evidence suggest some possible functions of cirRNAs in brain: because of their stability they are good candidates to work as platforms for RNP granules assembly or for RNAs and proteins transport to synapses [52]. Nevertheless, it is still unclear how circRNAs overexpression co-exists in brain with the upregulation of ADAR1, which via A-to-I editing of intronic complementary sequences, inhibits intronic base pairing thus suppressing circularisation [43] [52].
CircRNAs can also be packaged into vesicles and released at synaptic level, possibly providing a cell-to-cell messaging system. Indeed, circHIPK3, circZKSCAN1, circASXL1 and circKIAA0182 were found to be secreted in extracellular vesicles such as exosomes and micro-vesicles, that might both work for a cell-to-cell communication or might provide a clearance mechanism to regulate circRNAs levels in human cells (fig. 2G [64]).
Moreover, many studies indicate that circRNAs can potentially play an important role also at the pathological level. Indeed, CDR1as, the best-characterised circRNA up to now, is specific for neuronal tissues, where it acts as a sponge for miR-7 and, its expression is significantly reduced in Alzheimer's disease [65]. In addition, a group of circRNA has been recently characterised to be regulated by FUS, one of the main actors of familial ALS onset [40]. Besides neuronal diseases, hundreds of circRNAs were found to be regulated during epithelial to mesenchymal transition, suggesting that they could have a role in migration and cancer metastasis [38] and were also found to be involved in induction of innate immune response, with a characterised mechanism of recognition between self- and non-self-circRNAs [66].

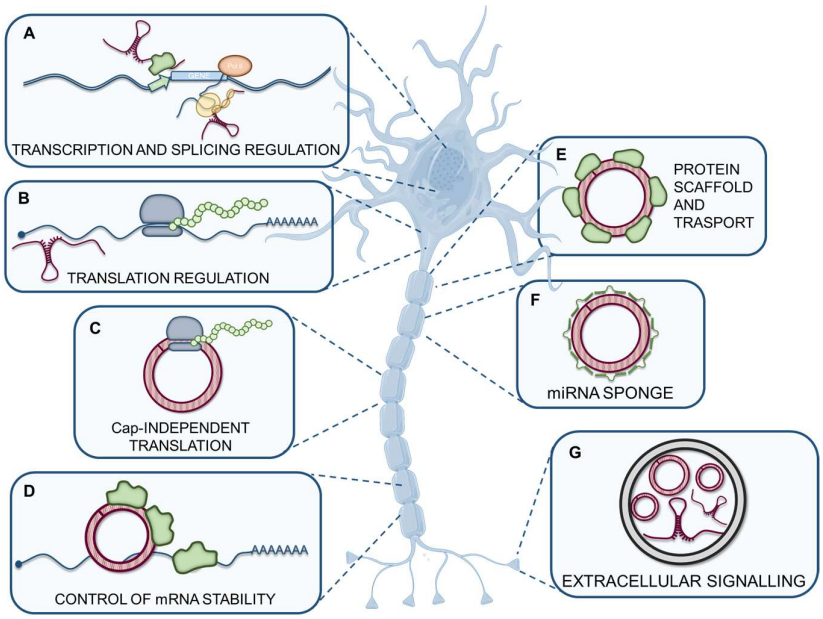

Figure 2: Mechanisms of action of non-coding RNAs

A) *LncRNAs can regulate transcription of specific genes binding transcription factors or recruiting transcriptional activator or repressors to promoters. Moreover, they can induce preferential inclusion or exclusion of exons, affecting mRNA splicing.* ***B and D)*** *ncRNAs can interact with mRNAs modulating their stability and controlling their translation.* ***C)*** *circRNAs and lncRNAs can contain a small ORF that can be translated into functional micropeptides. In particular, circRNAs can be translated in a Cap-independent manner as the ORF can be generated only upon circularization of the transcript.* ***E and F)*** *ncRNAs can bind microRNAs (miRNAs) or RNA binding proteins shuttling them to the cell periphery or sequestering them acting as a sponge.* ***G)*** *lncRNAs and circRNAs can be enclosed into extracellular vesicles and delivered for cell-to-cell communication in response to neuronal stimuli.*

3.2 Amyotrophic Lateral Sclerosis

Amyotrophic Lateral Sclerosis is a neurodegenerative disorder characterised by the progressive loss of motor neurons functions [67].
It can affect both upper motor neurons, that project from the cortex to the spinal cord/brainstem, and lower motor neurons, from the spinal cord/brainstem to the muscle [68].
A sporadic form of the disease, which shows no genetic onset, typical instead of the familial type of ALS, affects most of the patients. The total incidence of the pathology in Europe interests around 2-3 people over 100'000, with a 90-95% and 10-5% of cases, respectively associated to the sporadic and the familial form [69] [70]. In most of the cases, ALS symptoms, that include muscle weakness, twitching, cramping, swallowing difficulty and eventually muscles impairment [71] [72], appear between the age of 50 and 65, with a small minority of reports in people younger than 30 [73].
At the histological level, central and peripheral motor neurons undergo a degenerations process, possibly driven by apoptosis [74]. Aggregation and accumulation of protein inclusions are peculiar of the disease, even if the mechanism is still under extensive investigation.
Moreover, together with progressive muscular and motor cortex atrophy, up to 50% of patients that suffer from ALS develop concomitant cognitive/behavioural impairment, often diagnosed as Frontotemporal Dementia (13%) and with apathy as the most prevalent symptom [75] [76]. This led the scientific community to reclassify the pathology from neuromuscular to neurodegenerative disorder.
Environmental factors can have a role in the onset of the pathology, too. People who chronically smoke cigarettes [77], as well as athletes, have higher risk of developing the disease compared to overall population [78] [79]. Moreover, a prolonged exposition to

agricultural chemicals, formaldehyde and heavy metals has been associated to development of ALS [77].

Thanks to the spreading of genome wide association studies (GWAS) and the advent of next generation sequencing techniques, the genetic background of familial ALS was identified [80]. The identification of the SOD1 mutation was soon followed by the discovery of more than 30 genes directly involved in major risk of ALS [81].
Among them, it is worth mentioning the most frequent ones, which account for 70% of cases of familial ALS: C9orf72, SOD1 and additionally TDP43 and FUS, which are involved in gene expression regulation and RNA metabolism processes such as transcription, splicing and non-coding RNAs processing (fig. 4).
The most frequent genetic mutation in ALS patients is found in the SOD1 gene. SOD1 is a superoxide dismutase with antioxidant activity [82] and when mutated it is prone to form aggregates in motor neurons cytoplasm [81].
Accumulations of misfolded SOD1 were found on the cytoplasmic face of the mitochondrial outer membrane, suggesting that SOD1 mutation can have a role in the alteration of mitochondrial functions, such as ATP production and calcium homeostasis (fig. 3C, [83] [84]). Interestingly, defects in both anterograde and retrograde axonal transport are directly connected to mitochondria impairment [82] [85], often leading to motor neurons degeneration due to accumulation of mitochondria and autophagosome at the level of neurofilaments [86].
It was also proposed that limited substrate delivery to autophagosome could contribute to motor neuron degeneration, as C9orf72 is known to be a master regulator of autophagy [87]. C9orf72 mutations can also provoke defects in nucleocytoplasmic transport [88] [89], while endosomal and vesicle transport defects are typical of TDP43 degeneration (fig. 3C, [90]).

More recent studies enlightened the importance of RNA processing in ALS pathogenesis [91], as axonal mRNA transport is crucial for local protein translation. Specific examples are provided by mutations in the RNA binding proteins TDP43 and FUS [92]. ALS-linked mutations in TDP43 and FUS can lead to the alteration of up to 30% of whole transcriptome [93]. As a matter of facts, many ALS-linked mutation of these proteins result in their mis-localization from the nucleus to the cytoplasm, leading to a failure in processing their target RNAs, impairing transcription, splicing, microRNAs biogenesis and axonal transport [94] [95] [96]. Besides, the loss of function of RNA binding proteins in the nucleus can combine with a toxic gain of function when these proteins are prone to join stress granules and form aggregates in the cytoplasm (fig. 3E and fig. 4F, [97]).
Importantly, cell-to-cell propagation of the disease through a prion-like mechanism has been postulated for the progression of the disease linking ALS to tau and synuclein-derived pathologies [98] [99].
The synergistic cooperation of these cellular mechanisms ends in the failure for motor neurons to preserve axonal projections, leading to denervation of the muscles or loss of control on lower motor neurons. It remains unclear the reason why motor neurons are the most susceptible cell type to these mutations. In fact, even though maintaining long axonal projections seems to be the main trait of the disease, other neuronal subtypes that show even longer axonal projections do not seem to be compromised in the pathology [67].

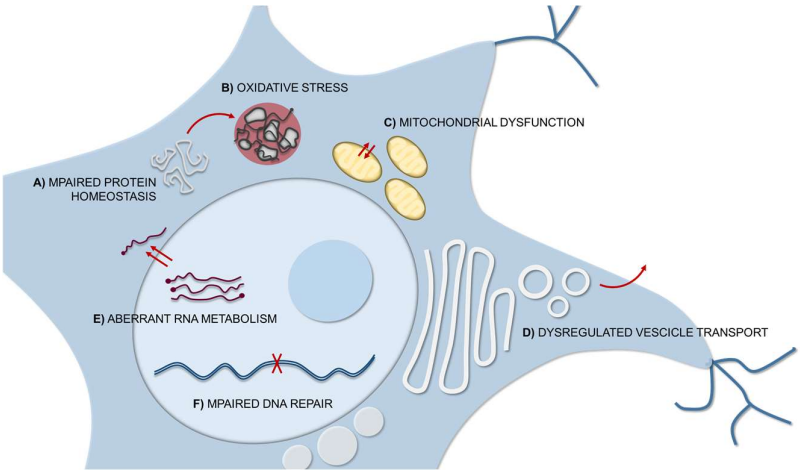

Figure 3: Pathophysiology of ALS

Mutations in several genes that have been implicated in the pathophysiology of amyotrophic lateral sclerosis (ALS) can impair motor neuronal functions through more than one pathophysiological mechanism. ***A and E)*** *Aberrant RNA metabolism, including impaired nuclear export and impaired protein homeostasis are predominant factors linking multiple ALS causative genes to neuronal injury.* ***B and C)*** *In particular, accumulation of misfolded proteins was correlated with chronic activation of oxidative stress and mitochondrial dysfunction.* ***D and F)*** *Moreover, other mechanisms can directly alter neuronal functions, such as impaired DNA repair and dysregulated vesicle transport.*

3.3 FUS' functions in phase transition

FUS/TLS (Fused in sarcoma/translocated in liposarcoma, here referred as FUS) was first identified as a fusion oncogene in liposarcoma. Its function is still under deep investigation, although it is known to be involved in several cellular processes such as proliferation, DNA repair, transcription regulation and RNA processing [100].

Normally, the protein is localised in the nucleus and, if necessary, can shuttle in the cytoplasm to exploit its functions [101]. In the

nucleus, FUS influences transcription of different target genes binding directly to their promoters [102], [103] or associating with nuclear hormone receptors, transcription factors and RNA polymerase III. Moreover, it collaborates in transcription initiation interacting with Pol II and the TFIID complex [102] and it is involved in the preservation of genomic integrity in the response to DNA damage (fig. 4A [104] [105]).
FUS was also identified as a component of the spliceosome machinery [106] [107] as it can bind the 5' and the 3' splice sites of pre-mRNA [108] and can regulate its own expression by alternative splicing [109] [110] and it participates in the Drosha complex, required for microRNA biogenesis (fig. 4A, [111] [112]).
In the cytoplasm, FUS is involved in different aspects of RNA metabolism, like subcellular localisation, translation and degradation (fig. 4D, [101] [113]). It re-localises in the cytoplasm upon inhibition of RNA pol II transcription [101] and, under stress conditions, joins cytoplasmic stress granules (fig. 4B, [114]). Interestingly, upon precise neuronal stimuli, it is involved, in the transport of specific mRNAs to dendritic spines in RNA-transporting granules, regulating neuronal plasticity by altering mRNA content and local translation (fig. 4C, [115] [116]). Furthermore, its association with the N-methyl-D-aspartate receptor-adhesion protein signalling complex suggests its involvement in mRNA translation regulation at the level of excitatory synapsis [117] and it may be involved in actin reorganisation in spines, as it can bind mRNAs encoding actin-related proteins (fig. 4D, [115]). It was also found to regulate microtubule growth in rat hippocampal axons [118] and was detected at the level of synapses in rat motor neurons [119]. Finally, supporting the hypothesis that FUS may regulate synaptic and neuronal plasticity, it was recently proved that FUS depletion affects the biogenesis of circRNAs [40] that, indeed, are highly enriched in neuropil and dendrites, acting on a post-transcriptional level, enhancing or repressing the back-splicing reaction.

Notably, RNA-binding proteins such as FUS, as well as TDP-43, are able to undergo liquid-liquid phase separation (LLPS) *in vitro* [120] [121] [122]. In LLPS, two separated liquid phases, one at higher and one at lower concentration, coexist in the same solution. In response to different stimuli, specific membraneless compartments can arrange, incorporating RNA and RNA-binding proteins into ribonucleoprotein (RNP) granules, with unique composition and functions. Importantly, many cellular functions of FUS are related to its ability to phase-separate, but aberrant phase transition from liquid to solid state can be a hallmark of ALS and FTD (fig. 4F, [123]).
RNA recognition motifs (RRM) of RNA-binding proteins are key players in RNPs formation: indeed, RNA can drive TDP-43 and FUS LLPS with sequence- and length-specificity and different concentrations of RNA could promote or inhibit FUS assembly [124] [125], [126].
In addition to RRMs, the N-terminal of FUS also contains a prion like domain (PrLD), a low complexity domain included in the IDRs (intrinsically disordered regions) category. PrLDs are enriched for asparagine, glycine and tyrosine residues [127] and, due to their lack of high-order structure, were demonstrated to be a major driver of protein phase separation [121], [125] [128] [129] [130].

Bio-molecular condensates deriving from LLPS can act as factories for accelerated enzymatic reactions or can sequester RNAs and proteins in response to specific signal cascades. For example, in response to DNA damage, FUS joins the nucleoli of spinal motor neurons [131], while it was found in the core of paraspeckles and is necessary for their formation in HeLa and SH-SY5Y cells [132]–[134].

Importantly, ALS/FTD-associated proteins are also recruited into stress granules (SGs) and, when mutated, can impair their proper dynamics and functions (fig. 4B and F).

Stress granules are non-uniform aggregates, as they are composed by internal sub-structures with high density of proteins and mRNAs, defined as “cores”, surrounded by a more dynamic “shell” [135]. FRAP (fluorescence recovery after photobleaching) experiments pointed out that components of the shell can exchange more rapidly, undergoing phenomena of fusion and flow in the cytosol [136]. 50% of the “cores” content is composed of RNA binding proteins, while the remaining half includes post-translational modification enzymes, metabolic enzymes, remodelling complexes and components of signalling pathways. However, the SGs composition is highly variable, depending on the type of stress the cell is undergoing [137].
In general, a variety of stress stimuli induce a broad translational silencing initiated by polysome disassembly, thus releasing polyadenylated mRNPs that can aggregate to form SGs or assemble in processing bodies (PBs) [138]. Ribosome dissociation is the result of a complex signalling cascade involving the accumulation of phosphorylated eIF2a, which is a core component of SGs [139]–[141]. The translational silencers TIA1 and TIAR are recruited to mRNPs and contribute to this translation arrest, enhancing polysome disassembly and aggregation of mRNPs [142]. On the other hand, G3BP and its molecular partner USP10 also regulate SGs assembly, possibly deubiquitylating mRNP components and facilitating their aggregation [143].
Nevertheless, the mechanism of assembly is context specific, suggesting that SGs can exert different functions depending on the stress they are induced by. For example, G3BP1 (Stress Granule Assembly Factor 1) and G3BP2 interaction with RNA is fundamental for SGs formation in oxidative stress, while they are not required during osmotic stress [144] [145]. On the other hand, some redundant components can be found in stress granules assembly such as Atx2/Pbp1 and TIA1/Pub1, although they are not fundamental for the process [146].

Moreover, post-translational modifications such as methylation, phosphorylation and glycosylation can influence SGs assembly, as they can alter protein-protein and protein-RNA interactions [147].

Stress granules are thought to fulfil several functions: first of all, they might enhance some biological reactions locally concentrating specific molecules. For example, Moon et al., 2019 [148] and Mateju et al., 2020 [149] demonstrated that, although most of the mRNA recruited in SGs are in a "stalled preinitiation complexes" [137], [150] [151] [152], 60S ribosomal subunit can also be recruited and mRNAs can undergo translation. On the other hand, as SGs increase in size under stress conditions, they can act like transient capacitors, storing untranslated mRNA that exceed the capacity of the translation and decay machineries [114].
Interestingly, some RNA granules can move along microtubules with a motor-dependent mechanism [153], possibly delivering mRNAs to specific sites in the cell for later activation, increasing their potentiality of post-transcriptional control on mRNAs. Moreover, in somatic cells, SGs contain miRNAs and Argonaute protein, supporting the hypothesis that they may have a role in translation and decay regulation [154].

Alterations in stress granules formation were mainly observed in degenerative diseases such as ALS and FTD, where mutations in RNA binding proteins determine the assembly of stress granule-like structures even in the absence of stress, while mutations in autophagy related genes impair stress granules clearance [155]. Both the mutations can lead to accumulation of stable beta-amyloid structures, whose irreversible accumulation can alter RNA biogenesis, signalling pathways and cytoplasmic transport, finally triggering cell degeneration and death (fig. 4, [155], [155], [156]).
Specifically, most of FUS's mutations correlated with ALS are missense and located preferentially in the 3' region of the transcript [60], [157]. NLS mutations, such as the P525L mutation, reduce the nuclear import, increasing the cytosolic concentration of FUS, while

prion-like domain mutations increase the aggregation potential of FUS, sequestering the protein into skein-like structures. As a result, FUS forms abnormal insoluble aggregates in the cytosol that can eventually join stress granules, affecting RNA metabolism and exerting a toxic effect in brain and spinal cord cells affected by ALS (fig. 4, [3]).

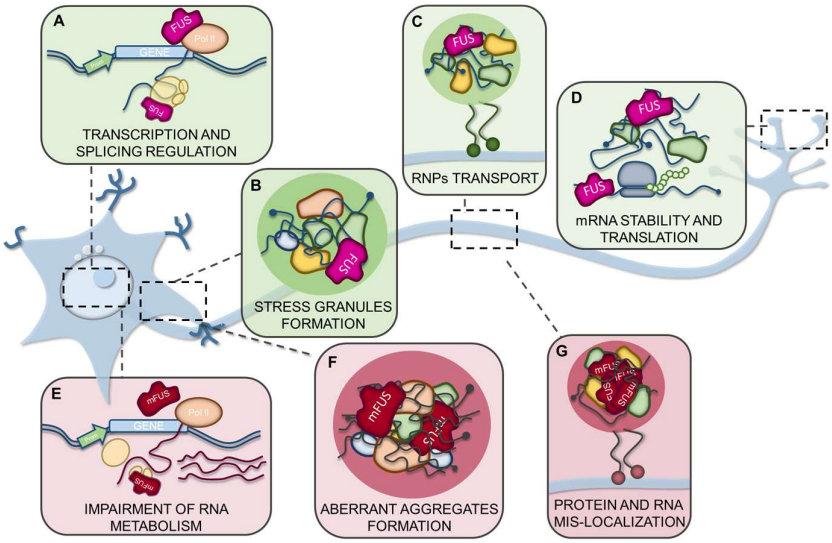

Figure 4: Proposed physiological roles of FUS.

FUS is a nuclear protein that, if necessary, can shuttle in the cytosol to exert its functions. ***A)*** *FUS can be recruited in the promoter region for transcriptional regulation, or, alternatively, can participate in the general transcription machinery associating with TBP and RNA pol II. Moreover, FUS was identified as part of the spliceosome and can indirectly bind structural regulatory elements on the downstream intron to promote exon inclusion.* ***B)*** *FUS is incorporated in stress granules where it forms complexes with other RNA binding proteins and mRNAs.* ***C and D)*** *FUS can travel in RNPs for the transport of RNAs along axons. Indeed, it was proven to shuttle mRNA to dendritic spines, where it may facilitate local translation.* ***E)*** *FUS's mutations causing its de-localization in the cytoplasm might result in the loss of its nuclear functions, leading to de-regulation of gene expression and splicing impairment.* ***F and G)*** *FUS's mutations in its NLS can cause its accumulation in the cytoplasm driving the formation of aberrant*

insoluble aggregates and compromising the proper transport of mRNA to the appropriate compartments, eventually causing a toxic gain of function.

3.4 Tools for imaging RNA

Understanding in how RNA undergoes complex and dynamic biochemical processes is constantly evolving, as mechanisms from mRNA transport, processing, translation, to degradation have been widely characterized [158] [159] [160]. However, the full comprehension of how RNA localization and dynamics affect their function, particularly for ncRNAs, is largely undefined.
In this context, RNA imaging technologies have been rapidly developing for both fixed and live cells. Taking advantage of the most recent innovations in fluorescent microscopy, scientists have been able to resolve the localization of the whole transcriptome and to achieve single molecule precision in fixed cells. On the other hand, also in live-cell imaging, even if still limited to single gene per colour, astonishing improvements in temporal resolution and in variety of live-cell RNA imaging tools has significantly advanced our understanding of the dynamics of RNA processing [161].

Fluorescent in situ hybridization of RNAs

Fluorescence *in situ* hybridization (FISH) is the most common technique for investigating RNAs localization, compartmentalization and abundance in fixed cells or tissue sections. It is a macromolecule recognition technology based on the complementary nature of nucleic acids. Fluorophore-coupled nucleotides can be incorporated in DNA strands and used as probes to hybridize complementary DNA or RNA sequences in cells and tissues, to be then visualised via imaging systems [162].
Starting from 1982, when Singer and Ward detected actin mRNA for the first time [163], FISH technique has been constantly upgraded over the years: worth mentioning, in 2008 Raj and colleagues achieved single-molecule FISH (smFISH) targeting

specific mRNAs with a set of 48 probes, each conjugated to a single fluorochrome (fig. 5A, [164]).
Later, rolling circle amplification (RCA)-FISH was also developed: in RCA, complementary DNA of the whole transcriptome is generated *in situ* with reverse transcription. mRNAs are then degraded by ribonuclease H and padlock probes are hybridized to targeted cDNA. The padlock probes serve then as a template for rolling circle amplification by DNA polymerase and, at last, probes specific for each padlock are hybridized and visualized [165][166]. This technique was even enhanced combining optical super-resolution microscopy and combinatorial labelling to measure mRNA levels of several genes simultaneously in single cells [167].
In *combinatorial FISH,* each mRNA is barcoded with unique "spectral barcode" by sequential rounds of hybridization, imaging and probe stripping for multiplex different mRNA quantitation. The multiplexing capacity scales up as the number of fluorophores and rounds of hybridization increases [167].
Finally, techniques such as RNAscope and click-amplifying FISH (clampFISH) are based on series of primary, secondary and tertiary oligonucleotide probes hybridized sequentially to enhance fluorescent or chromogenic signal (fig. 5B, [168], [169]). These probes provide massive amplification as they allow a maximum of 8000 fluorophores for 1 Kb target RNA [169], however, the huge pre-amplifier and amplifier probes might have difficulties penetrating the complementary sequences of mRNAs bound to RNP complexes, as proteins may cause steric hindrance [170].
Importantly, RNA-FISH has been extensively used to image non-coding RNAs [171]–[173], and RNAscope was recently exploited to visualize circular RNAs targeting the back-splicing junction, thus guaranteeing specificity for the circular isoform (reviewed in [174] and in [175]).

Live-cell RNA imaging

In the years, a lot of effort was also spent on developing tools for imaging RNAs in live cells. Indeed, while advances in RNA FISH allowed reaching great outputs in terms of spatial resolution and multiplexing, a lot of information is missing if it comes to study the RNA dynamics. Several approaches have been proposed for both endogenous and exogenous RNA detection. Most of these tools take advantage of RNA binding proteins that can be fused to a fluorescent molecule, like a fluorescent protein (FP) to target an RNA of interest [161], [176]. Fluorogenic RNAs are also spreading fast for exogenous RNAs detection, while chemically synthesized probes and genetically encoded probes were developed for endogenous RNAs targeting [161]. Below, the most relevant live-cell RNA systems are listed and briefly described.

- RNA stem-loop systems

The MS2 system was pioneered by the Singer Lab in the 1990s and remains the most widely used RNA imaging system today. It was developed from MS2 bacteriophage coat protein dimers (MCP), 129-amino acids long proteins able to form homodimers and to bind 21-nt long RNA stem loops (abbreviated MS2) with a conserved loop region and bulge [177], [178]. Typically, a series of MS2s is appended to the target RNA to serve as the recognition element and each MCP is fused to an FP for visualization (fig. 5C, [179]).
Analogous systems to MS2 are PP7 system, developed from PP7 bacteriophage coat protein dimers [180] and λN imaging system, developed from bacteriophage λN protein [181].
In the last years, many improvements on the first generation of MS2/PP7 systems have been elaborated, to avoid repetitive sequences, to enhance the signal-to-noise ratio [182] and to reduce background due to unbound fluorescent protein [183]–[185]. The MS2/PP7 systems have been extensively used to track the dynamics of mRNA processing as they are relatively resistant to

photobleaching and the 48 GFPs bound on each mRNA guarantee high signal-to-noise ratio [186], [187].

- Fluorogenic RNAs

The first custom dye-binding RNA aptamer to see wide recognition, Spinach, was developed by Jaffrey and colleagues using a fluorophore that mimicked the structure of GFP [188]. The approach exploits the fact that the GFP chromophore is non-fluorescent outside of the protein but becomes fluorescent upon binding to the aptamer due to rigidification (fig. 5E).
In general, initial aptamers are isolated via sequential rounds of SELEX. Later, fluorescence assay (via bacterial cell sorting) further improve the absolute brightness of the probe, thus producing a new aptamer [189].
Other groups have built on this concept of fluorophore rigidification by developing their own small molecule with accompanying aptamers. For example, Unrau and colleagues took advantage of thiazole orange (TO1) that was known to bind double-stranded nucleic acids [190], [191]. The aptamers developed for these fluorophores (termed Mangoes) were tighter binders and more red-shifted than Spinach. Mango's improvement over Spinach is due to its increased thermal stability upon binding the TO1-B substrate [192]. Recent research from Unrau and colleagues has shown that arrays of Mango II aptamers can be used to image mRNA granules in live mammalian cells, and single lncRNAs in fixed cells [193]. One potential limitation of the Broccoli, Spinach and Mango systems is the presence of G-quadruplexes in the aptamer structure. This structure has been found to be crucial for fluorophore rigidification in the aptamer. However, it is increasingly recognized that such secondary structures are actively degraded in mammalian cells [194].
The newest family of dye-binding aptamers, Peppers, takes a step toward resolving the main issues that plague Spinach/Broccoli/Corn and Mangoes. The Peppers aptamer binds a series of custom small molecules with a stilbene core inspired by GFP and named ‘‘HBC’’,

as an abbreviation for the IUPAC name. Developed by Yang and colleagues [1] with the goal of solving the outstanding issues of aptamer degradation and fluorophore brightness, the authors selected a new aptamer that does not contain a G-quadruplex. The most well vetted small molecules able to bind Pepper aptamer are HBC530 and the red-shifted HBC620. When compared with other fluorophore-aptamer pairs, Pepper530 demonstrated 9- and 11-fold higher signals than Broccoli and Corn in mammalian cells. mRNA tandem-labeled with 4xPepper and 4xMS2 revealed that Pepper530 outperforms MCP-mCherry, and Pepper620 outperforms MCP-GFP in signal-to-noise. It was also shown that Peppers could be used to image a wide range of different classes of bulk RNAs.

- dCas13

The dCas13 system was developed from CRISPR/Cas13. In this technique, the guide RNA (gRNA) of Cas13 binds a target RNA by hybridization and the target RNA is cleaved by Cas13 enzyme [195]. In the imaging system, a variety of catalytically dead Cas13 (dCas13) fused to eGFP were screened with a gRNA for recruitment to a known target RNA location (fig. 5D). Unlike the systems mentioned above, this tool enables detection of endogenous untagged RNAs. Eight tandem gRNAs for eight tandem dCas13-eGFP fusion proteins is sufficient for single-molecule live-cell imaging. In addition, dCas13 proteins from two different species can be used orthogonally to monitor two target RNAs or two regions of the same target RNA. By qPCR, the dCas13 imaging system does not decrease transcription of the target RNA unlike MS2, but other perturbations, such as translational efficiency have not been tested yet [196].

- Chemically synthesised molecular beacons

Molecular beacons are oligonucleotide-based probes with a stem-loop: the sequence in the loop is designed to hybridize with an endogenous RNA of interest, and the termini are modified with a fluorophore and a quencher (fig. 5F, [197]). These probes are dark

in the unbound state because the quencher is held in proximity to the fluorophore, but beacon unzipping and fluorescence turn-on occur upon hybridization with the target RNA. The first molecular beacon was developed by Tyagi and Kramer in 1996 [198] and the technology was adapted for use in live cells in 2003 by creating nuclease-resistant beacons [199]. Recent work has shown that such probes can also be used to track single RNAs in live neurons [200].

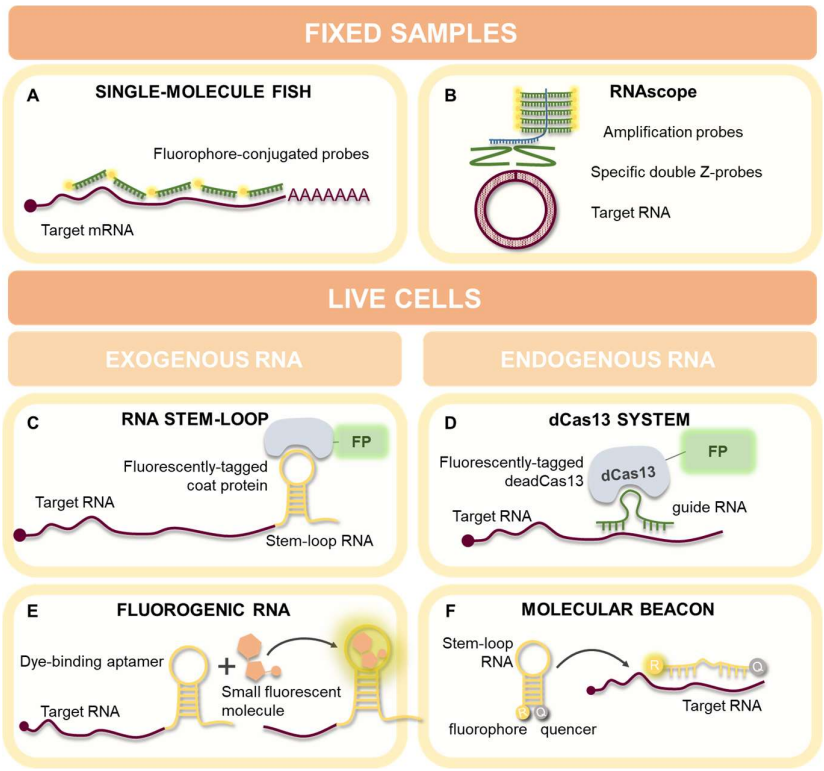

Figure 5: Tools for imaging RNAs.

Many techniques have been developed for the detection of RNA molecules in fixed tissues and in fixed or live cells. ***A)*** *Single-molecule FISH is the most widely used technique for detecting RNAs in fixed cells or tissue sections. Fluorophore-coupled probes are hybridized on specific RNA sequences in cells and tissues, to be then visualised via imaging systems.* ***B)*** *RNAscope FISH relies on series of*

primary, secondary and tertiary oligonucleotide probes hybridized sequentially to enhance a fluorescent signal. It is recommended to detect splicing-isoforms, such as circularRNAs, or single nucleotide variants, as only two sequence-specific probes are required for hybridization on the target RNA. ***C)*** *RNA stem-loop systems, such as MS2 system, allow the detection of exogenous RNAs in live cells. These tools are based on a coat protein that can bind an RNA stem-loop. A series of stem-loops is added to the target RNA and each coat protein is fused to a FP for visualization.* ***D)*** *The dCas13 imaging system allows the detection of endogenous RNAs in live cells. Cells express a catalytically dead Cas13 (dCas13) fused to an eGFP that is recruited to a known target RNA thanks to a series of sequence-specific guideRNAs (gRNA).* ***E)*** *In Fluorogenic RNA based techniques, the sequence of an RNA of interest can be tagged with an RNA aptamer to observe its dynamics in live cells. The aptamer binds a small molecule that becomes fluorescent only upon binding to the RNA aptamer.* ***F)*** *Molecular beacons are oligonucleotide probes designed to hybridize with an endogenous RNA. The stem-loop is sequence-specific and the termini are modified with a fluorescent reporter (R) and a quencher (Q). When the beacon binds the target RNA, it unzips and fluorescence is turned-on.*

Overall, these applications are mostly suited for mRNA and sophisticated single mRNA tracking studies provided meaningful information to advance our knowledge about mRNA processes and cell biology. Nonetheless, fewer examples of tagging and tracking ncRNA are reported, possibly because of the higher levels of complexity that characterize them in either structure, classes and size and this might raise concerns about perturbing their function when introducing a tag.

4. AIM OF THE STUDY

The study of RNA dynamics in live mammalian cells is gaining more and more importance to understand many aspects of cell functioning, both in physiology and in disease onset and progression. Indeed, the spatial organization of the transcriptome is a crucial aspect for the regulation of gene expression, especially in highly polarized cells such as motor neurons (MNs), where transcripts and proteins must be properly transported along axons and dendrites to exert their functions. The importance of mRNA localization is a well-known fact, however in the last decades, the discovery of different classes of ncRNAs and their mechanism of action have increased researchers' awareness on their crucial role in many layers of cell biology, including RNA and protein metabolism, RNPs transport and extra-cellular signalling. Among ncRNAs, circRNAs, a recently discovered class of covalently closed RNA molecules, have become subject of intense studies. They are highly enriched in neuronal tissues, particularly in synapses, suggesting that they can have a role in neuronal plasticity and/or transport of RNA and proteins. Given the growing interest in understanding RNA dynamics, scientists have developed many different techniques to assess RNA transport and localization in live cells, such as, the use of fluorescent proteins, RNA aptamers or fluorescent probes.

Nonetheless, there are no examples in literature of research groups performing live imaging experiments in mammalian cells on naturally occurring circular RNAs. Indeed, they are usually low abundant molecules, that upregulate only in specific time windows during development [52], [201]. Moreover, the back-splicing junction is the only specific sequence that allows distinguishing between a circular RNA and other linear isoforms deriving from the same pre-mRNA. Altogether, these features makes them challenging to target both in fixed and in live cells [174].

In this work, two circular RNAs, circ-Dlc1 (from now on referred as circ-16) a circular RNA deriving from the back splicing of exon 2 of Dlc1 (deleted in liver cancer-1) gene and circ-Hdgfrp3 (from now on referred as circ-31) generated from the circularisation of exons 2-5 of Hdgfrp3 (Hepatoma-Derived Growth Factor-Related Protein 3) gene and one long non-coding RNA, HOTAIRM1, were selected as attractive targets. In fact, they are all highly expressed upon spinal motor-neurons differentiation. Moreover, circ-16 and circ-31 biogenesis depends from the ALS-related pleiotropic protein FUS [40], while HOTAIRM1 directly interacts with FUS [202], prompting speculations about their involvement in ALS onset.
Importantly, in D'Ambra et al., 2021 [2] combination of fluorescent *in situ* hybridization with immunofluorescence allowed to demonstrate that circ-31 mostly traffics along neurites, while upon oxidative stress it is retained in the perinuclear region. In particular, upon oxidative stress stimulus, circ-31 localizes in stress granules (SGs) in wild-type MNs, and an even higher proportion of circ-31 is trapped into cytoplasmic aggregates in MNs carrying FUSmut.

Given these premises, I focused on the development of an effective strategy to visualize those targets in live mammalian cells. Hence, we decided to take advantage of fluorescent RNA tags, specifically of the newly developed Pepper [1], in order to follow circ-16, circ-31 and HOTAIRM1 dynamics in association with the stress granules marker G3BP1 and with the ALS-related protein FUS, possibly adding novel layers of information about their behaviour in physiological and pathological conditions.

5. RESULTS

Engineering and validation of overexpression constructs for circRNAs live imaging

CircRNAs are a novel and still poorly investigated class of non-coding RNAs whose functions, except from a few cases, are still unknown. Nevertheless, transcriptomic studies shown that they are widely enriched in nervous system [52], opening to an intriguing possible involvement in neurodegenerative diseases. Interestingly circRNAs are often observed at the periphery of cells, furthermore a possible role in RNP granules assembly and transport along axons and to synapses was hypothesized [52]. In this context, investigating their subcellular localization and determining their dynamics would be of great support to interactomics and transcriptome analysis, specifically when it comes to study proteinopathies that are known to disrupt axonal trafficking, such as ALS and FTD.
With this background, it seemed crucial to study their association to phase separation events, specifically in the dynamics of ALS-related condensates, such as stress granules and aggregates formed by FUSmut. To do that, we decided to set up a strategy to image circular RNAs in live mammalian cells, so that we could be able to follow their interaction with SGs and ALS markers.

In order to address this demanding goal, we decided to take advantage of one of the newest family of dye-binding aptamers, Pepper [1]. Indeed, Pepper is very short if compared with previously described fluorescent RNAs (fRNAs) and a limited tandem of units can provide optimal signal to noise ratio, overall consisting in an ideal tool to target short-sequenced non-coding RNAs that mostly relies on their structure rather than their sequence to exert their functions.
To optimize the expression of circular RNAs tagged with the fRNA, a doxycycline-inducible plasmid able to enhance the production of circRNAs (here referred as p-circ) was engineered. As described by

Kramer and colleagues and in Legnini et al, 2017, circular RNAs over-expression can be boosted exploiting a vector containing inverted complementary sequences (ICSs) flanking the circRNA sequence (fig. 6A, [39] [62]). Indeed, complementary base pairing of ICSs can mimic the role of intronic sequences in the genome, physically drawing together the 5' splice site and the 3' splice site and promoting the formation of the back-splicing junction.
Hence, the sequences of circ-31 and of circ-16 were cloned between the ICSs of the p-circ overexpression construct, generating p-circ31 and p-circ16 plasmids.
Secondly, to tag the circular RNAs with the fRNA, two different insertion sites were selected for each circRNA. The main concern was not to disrupt the back-splicing junction, nor to perturb the circularization efficiency of the construct, hence we decided to integrate the sequence of Pepper in two arbitrary insertion sites at least 50 nucleotides away from the 5' or the 3' splice site. Thus, four repetitions of Pepper were cloned in the final constructs p-circ31_site1 and p-circ31_site2, respectively within exon 4 and exon 5, while eight repetitions of Pepper were inserted in p-circ16_site1 and p-circ16_site2 within exon 2.
The number of units to integrate in each circular RNA was established trying to optimize the balance between signal to noise ratio and target perturbation: Chen et al, 2019 [1] defines that the fluorescence of Peppers increases linearly with the number of in tandem arrays up to eight. Consequently, as circ-16 is 1148 bps long, we decided to tag it with eight units of Peppers, as they consist of 360 bps in total. On the other hand, as circ-31 is only 522 bps long, we integrated only four arrays of Pepper (196 bps), to avoid excessive perturbation of the circular RNA structure.

Once engineered all the p-circ constructs, the over-expression level, the circularization efficiency and the localization of the transcripts were evaluated, in order to assess if the fRNA tag could impair any of these events. Indeed, coupling of the ICSs of p-circ plasmid is a co-transcriptional process that does not occur with 100% efficiency,

but can be affected by the length of the circular RNA and the length of the ICSs [39]. Hence, this could result in a different proportion between properly circularized transcript and a spurious linear non-circularized transcript (here referred as "precursor") composed of the ICSs, the exons of the circular RNA, the fRNA and canonical 5'-cap and poly-A tail (fig. 6A), that retains the ability to bind the fluorescent dye just like the tagged circular RNA and could be responsible for an unwanted fluorescent signal.
For that reason, in the first place qPCR was performed upon transfection and doxycycline induction of HEK 293T cells, to determine the expression level of both circular and precursor isoforms. HEK 293T cells were selected to conduct the following experiments since they exhibit high transfection efficiency and are widely used for functional characterizations of proteins [203]–[205]. To distinguish between the two isoforms, divergent primers were designed to amplify the BSJ of circ-31 and circ-16, while one primer on the ICSs and one primer close to the 5' end of circ-31 and circ-16 sequences were used to detect the precursor isoform (fig. 6B). To minimize biases given by PCR efficiency the reverse primer is common for both the targets. As shown in figure 6C, when inducing the TRE promoter with doxycycline, both the plasmids p-circ31_site1 and p-circ31_site2 result in a good over-expression of the circular isoform, even if p-circ31_site2 generates a higher amount of precursor if compared with p-circ31_site1. Importantly, p-circ31_site1 provides a good circular:precursor ratio, with the circular isoform being more abundant than the linear precursor. On the other hand, in figure 6D, the expression and circularization efficiency of p-circ16_site1 and _site2 are shown. Differently from the p-circ31 plasmids, p-circ16 constructs does not provide such an efficient overexpression of circular isoform, but they mainly result in linear precursor product, with an overall circular:precursor ratio suboptimal for further applications.

Considering the expression levels and based on the circular:precursor ratio, p-circ31_site1 and p-circ16_site2 were

selected to conduct further analysis to better characterize the impact of Pepper tag on circular RNA over-expression. As a matter of facts, it was then evaluated if the insertion of Pepper array could affect the proper localization of circ-31 and circ-16, given the assumption that both circular RNAs were described as mainly cytoplasmic [40]. Therefore, nuclear/cytoplasmic fractionation was performed on HEK 293T transfected with p-circ31_site1 and p-circ16_site2: as shown in figure 6E and F, exogenous circ-31 is mostly exported in the cytoplasm (58%), in accordance with the endogenous transcript. Importantly, most of the precursor isoform remains retained in the nucleus (63%), meaning that, if looking at a fluorescent signal in the cytoplasm when imaging Pepper, it will be predominantly supplied by circular molecules (72% of cytoplasmic transcript, calculated integrating overexpression levels of circular and precursor isoforms with their localization).
Besides, exogenous circ-16 is mostly cytoplasmic too (81%), but, regrettably, also the precursor isoform is preferentially found in the cytoplasm (74%), implying that the signal observed when imaging cells transfected with p-circ16 will be ambiguous, if not principally attributed to spurious precursor molecules.

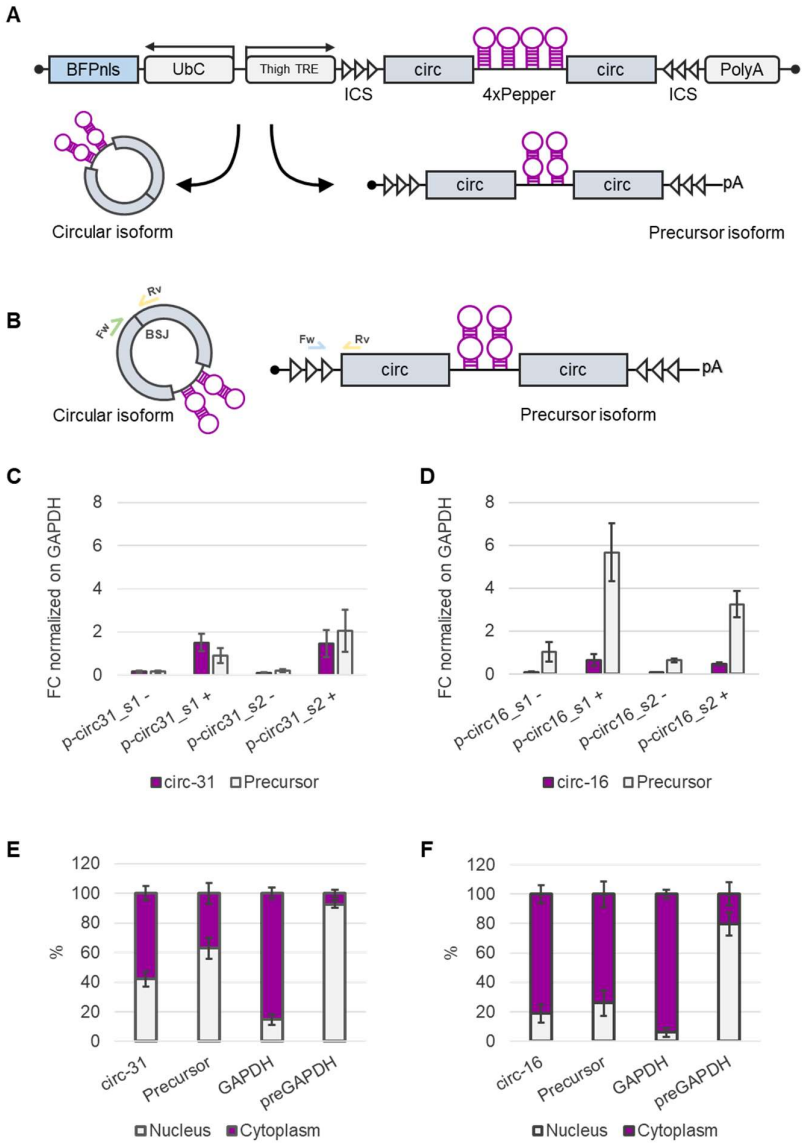
A
BFPnls
UbC
Thigh TRE
ICS
circ
4xPepper
circ
ICS
PolyA
Circular isoform
circ
circ
pA
Precursor isoform
B
Rv
Fw
BSJ
Circular isoform
Fw
Rv
circ
circ
pA
Precursor isoform
C
FC normalized on GAPDH
8
6
4
2
0
p-circ31_s1 -
p-circ31_s1 +
p-circ31_s2 -
p-circ31_s2 +
circ-31
Precursor
D
FC normalized on GAPDH
8
6
4
2
0
p-circ16_s1 -
p-circ16_s1 +
p-circ16_s2 -
p-circ16_s2 +
circ-16
Precursor
E
%
120
100
80
60
40
20
0
circ-31
Precursor
GAPDH
preGAPDH
Nucleus
Cytoplasm
F
%
120
100
80
60
40
20
0
circ-16
Precursor
GAPDH
preGAPDH
Nucleus
Cytoplasm

Figure 6: Overexpression constructs for exogenous circRNA visualization.

__A)__ Graphical representation of the over-expression plasmids designed to tag and visualize circular RNAs with fRNA Pepper. __B)__ Graphical representation of the primers used to assess circularization efficiency of p-circ plasmid series via qPCR. __C)__ Expression levels of circ-31_site 1, circ-31_site 2 and relative linear isoform upon doxycycline administration (+) normalized on GAPDH levels, quantified through qPCR. Error bars representing ± SEM (N=3). __D)__ Expression levels of circ-16_site 1, circ-16_site 2 and relative linear isoform upon doxycycline administration (+) normalized on GAPDH levels, quantified through qPCR. Error bars representing ± SEM (N=3). __E)__ Nuclear and cytoplasmic fractions of exogenous circ-31 and its relative linear isoform expressed in percentage. GAPDH and preGAPDH were used as cytoplasmic and nuclear controls, respectively. Error bars representing ± SEM (N=3). __F)__ Nuclear and cytoplasmic fractions of exogenous circ-16 and its relative linear isoform expressed in percentage. GAPDH and preGAPDH were used as cytoplasmic and nuclear controls, respectively. Error bars representing ± SEM (N=3).

Altogether, it was possible to engineer over-expression plasmids to tag the circular RNAs, circ-31 and circ-16, with an array of Pepper fRNA. While circ-31 proved out to be a feasible candidate to further investigate its dynamics, low circularization efficiency of the p-circ16 overexpression constructs discouraged us to carry on with additional experiments, requiring a complete re-design of the p-circ16 plasmids to increase transcription of circular isoform.

Visualization of circ-31 interacting with ALS-related RNPs in live mammalian cells

Once validated the feasibility of over-expressing circ-31 tagged with Pepper fRNA, the next step was to determine its interaction with proteins involved in phase-separation events, in the context of ALS. In fact, while in D'Ambra et al., 2021 [2] it was possible to describe circ-31 entrapment in pathological aggregates in fixed murine motor neurons, no information was provided about the dynamics and the timing of the process, neither on the sub-structural architecture.

Therefore, as circ-31 was found to co-localize with both wild type and pathological RNPs, we selected stable HEK 293T cell lines expressing either the stress granules marker G3BP1 tagged with GFP or the ALS-related protein FUS carrying the severe P525L mutation (FUSmut) always tagged with GFP, in order to follow circ-31 interactions with both proteins.
Hence, p-circ31 construct was transfected in HEK 293T cells as described above, and upon 48 hours of doxycycline induction, cells were treated with HBC 620 fluorogenic dye, to detect any signal from the over-expressed circular RNA. Notably, the p-circ plasmids were equipped with a tagBFP marker gene, adapted with a nuclear localization signal (NLS) (fig. 6A), so that transfection efficiency could be determined throughout the experiments.
Looking at the HBC fluorescent signal, most of the BFP positive cells show an intensity that cannot be isolated from the background noise, however a few cells in the sample exhibit an optimal signal-to-noise ratio, providing a nice fluorescent yield. As expected from the molecular characterization of the construct (fig. 6E), the fluorescent signal is mainly cytoplasmic and is not evenly distributed and diffused all over the cytoplasm, but looks confined in focal foci, possibly corresponding to specific sub-cellular compartments (fig. 7A).
Remarkably, when transfecting HEK 293T expressing G3BP1-GFP, a strong co-localization between the GFP and the HBC signal was observed, suggesting that circ-31 is recruited in G3BP1-positive RNP granules (fig. 7A). Therefore, single particle tracking was performed on selected Regions Of Interest (ROIs) on both circ-31 and G3BP1 signals, taking advantage of TrackMate plug-in on Fiji Image-J [206], [207].
In figure 7B, trajectories of G3BP1 and circ-31 of two representative particles in a single cell are plotted as a function of time. Imaging the particles for ~15 minutes at a temporal resolution of ~11sec/frame, we could follow their interaction frame by frame: circ-31 and G3BP1 signals intersect for most of the time, with occasional, but never complete, parting events. Interestingly, we

also observed merging events between particles over time (i.e. frame 00:01:06), a common phenomenon in liquid-liquid phase separation-based formation of membraneless compartments [208]–[210].
Moreover, since the dye HBC 620 is compatible with structured illumination microscopy (SIM), we super-resolved the localization of circ-31 in the bigger G3BP1-positive RNPs, which resemble stress granules in shape and size. As a matter of facts, as suggested by looking at the intensity map (fig. 7C, lower panel) and plotting the intensity profile of single RNPs for the signal of both HBC and GFP (fig. 7D), it appears that circ-31 localizes in the shell of such compartments, while, as expected, G3BP1 is more condensed in the core [135]. Overall, these observations provide interesting suggestions about the possible mechanism through which circ-31 is engaged in SGs upon oxidative stress induction. These analyses will be further validated in future experiments upon oxidative stress conditions.

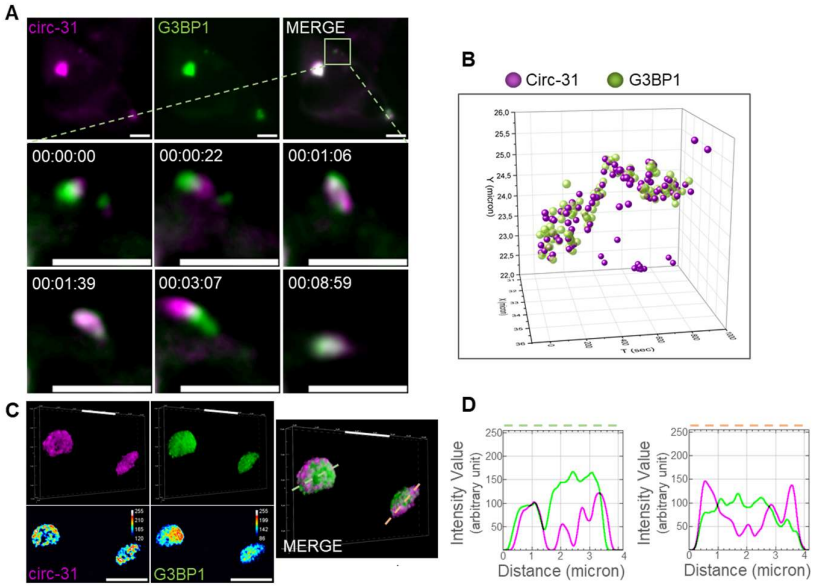

Figure 7: Exogenous circ-31 with G3BP1 in HEK 293T cells.

__A)__ Representative cell (N=2 biological replicates) imaged with a wide-field microscope expressing both circ-31 labelled with HBC 620 fluorogenic dye (magenta) and G3BP1-GFP (green). Lower panel shows a magnification view of two circ-31 and G3BP1 particles interacting over time (duration 15min; interval ~11sec). __B)__ Single particle tracking of circ-31 and G3BP1 over time. The plot indicates circ-31 (magenta) and G3BP1 (green) xy-coordinates (micron) as a function of time (sec). __C)__ 3D rendering of two representative RNPs containing circ-31 (magenta) and G3BP1 (green) imaged with 3D-SIM (structured illumination microscopy). Lower panels represent intensity map showing relative grey scale intensities of Z-projections. __D)__ Intensity value (arbitrary unit) of circ-31 (magenta) and G3BP1 (green) showing their signal distribution along a reference line crossing a representative SG. All scale bars correspond to 5 μm.

Afterwards, we also tested if the RNPs interacting with circ-31 also contain FUSmut, this time transfecting HEK 293T stably expressing FUSmut-GFP. Indeed, it is worth reminding that, in murine motor neurons mutant for FUS^{P517L} (equivalent to the human P525L), circ-31 is sequestered in pathological aggregates and that this leads to a strong impairment of its proper peripheral localization [2]. Said so, when looking at both circ-31 and FUSmut in live, transfected HEK 293T, a scenario quite similar to the one previously observed with G3BP1 is revealed: circ-31 co-localizes with FUSmut (fig. 8A) and again, when tracking single particles of both fluorophores, their interaction is persistent over time and they occasionally merge in bigger RNPs (fig. 8B). The continuous aggregation of FUSmut leading to the formation of pathological insoluble aggregates should affect in a detrimental way circ-31's functions. Interestingly, looking at bigger, spontaneous aggregates with SIM and plotting signal profile, circ-31 appears to be localized in the shell, while FUSmut, as well as G3BP1, also participates in the core structure (fig. 8C and D).

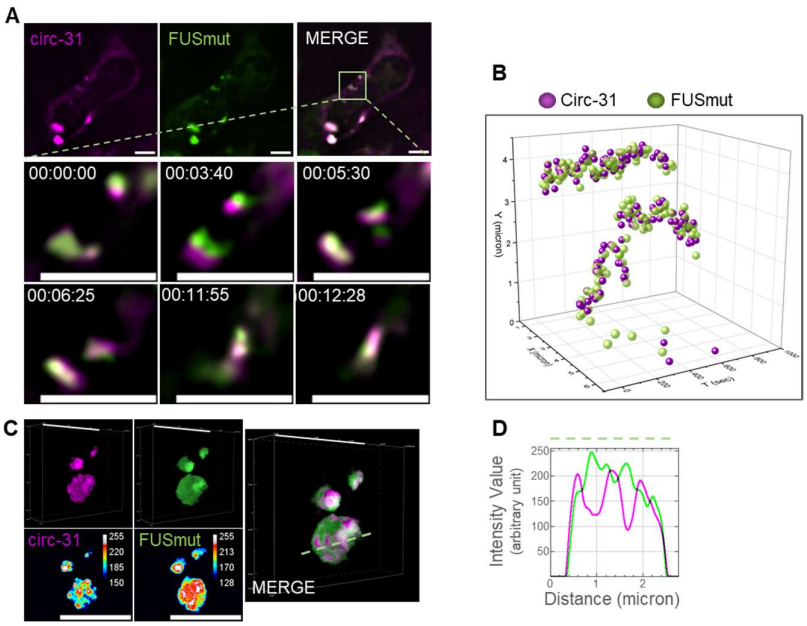

Figure 8: Exogenous circ-31 co-localizes with FUSmut in HEK 293T cells.

__A)__ Representative cell (N=2 biological replicates) imaged with a wide-field microscope expressing both circ-31 labelled with HBC 620 fluorogenic dye (magenta) and FUSmut-GFP (green). Lower panel shows a magnification view of two circ-31 and FUSmut particles interacting over time (duration 15min; interval ~11sec). __B)__ Single particle tracking of circ-31 and FUSmut over time. The plot indicates circ-31 (magenta) and FUSmut (green) xy-coordinates (micron) as a function of time (sec). __C)__ 3D rendering of two representative RNPs containing circ-31 (magenta) and FUSmut (green) imaged with 3D-SIM (structured illumination microscopy). Lower panels represent intensity map showing relative grey scale intensities of Z-projections. __D)__ Intensity value (arbitrary unit) of circ-31 (magenta) and FUSmut (green) showing their signal distribution along a reference line crossing a representative SG. All scale bars correspond to 5 µm.

circ-31 positive RNPs interplay with DCP1A marked processing bodies

Since G3BP1 marked RNPs, especially when it comes to stress conditions, are known to interact with other membraneless compartments [211], [212], we also wanted to test the association of circ-31 to other cytoplasmic organelles, to better characterize all the components that can be involved in its metabolism. Therefore, we started investigating circ-31 interaction with processing bodies (PBs), taking advantage of HEK 293T stable cell lines expressing DCP1A (decapping mRNA 1A) tagged with GFP. Indeed, PBs are cytoplasmic RNPs involved in post-transcriptional regulation of RNA, specifically in translation repression and decay [213]. Although not much is known about circular RNAs degradation, it is known that proteins involved in their decay such as GW182 and Ago2 localize in PBs [214], [215].
Intriguingly, tracking circ-31 positive RNPs and DCP1A, we observed a strong interplay between the two compartments over time (fig. 9A), finding a persistent association both in time (fig. 9B) and, through SIM-resolved acquisitions, in space (fig. 9C and D).

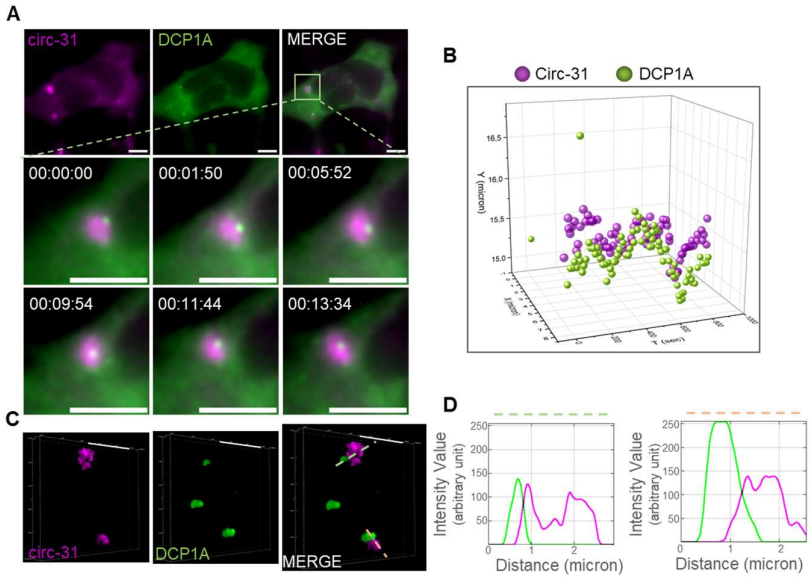

Figure 9: circ-31 positive RNPs co-localize with DCP1A tagged PBs in HEK 293T cells.

__A)__ Representative cells (N=2 biological replicates) imaged with a wide-field microscope expressing both circ-31 labelled with HBC 620 fluorogenic dye (magenta) and DCP1A-GFP (green). Lower panel shows a magnification view of an RNP containing circ-31, interacting with DCP1A tagged PBs (duration 15min; interval ~11sec). __B)__ Single particle tracking of circ-31 and DCP1A over time. The plot indicates circ-31 (magenta) and DCP1A (green) xy-coordinates (micron) as a function of time (sec). __C)__ 3D rendering of two representative RNPs containing circ-31 (magenta) associated with DCP1A tagged PBs (green) imaged with 3D-SIM. __D)__ Intensity value (arbitrary unit) of circ-31 (magenta) and DCP1A (green) showing their signal distribution along a reference line crossing a representative SG. All scale bars correspond to 5 µm.

Hence, fRNA Pepper proved out to be a valid tool to image circ-31, as we were able to detect it in association with RNPs containing both G3BP1 and FUSmut, supporting the model of its sequestration proposed in D'Ambra et al., 2021 [2]. Importantly, this would represent the first case of an exogenous circular RNA imaged through a similar approach and visualized at a super-resolution

level. Moreover, we also observed a strong interplay of circ-31 positive RNPs with PBs, rising novel questions about its function and metabolism.

LncRNA HOTAIRM1 is recruited in physiological and pathological SGs and its ablation affects FUSmut aggregation

Together with circRNAs, also lncRNAs are subject of great interest in the fields of research involving neurodegeneration and liquid-liquid phase separation. In fact, different long non coding RNAs such as Norad and MALAT1 [216], [217] were found to be constituents of the SGs transcriptome and are thought to work as scaffolds for the first steps of SGs nucleation.
HOTAIRM1 is a long non-coding RNA highly expressed upon motor neurons differentiation that was proved to directly interact with FUS protein in the cytoplasm [202]. Indeed, in Rea et al., 2020 our collaborators demonstrated that HOTAIRM1 is mostly cytoplasmic, that FUS regulates its abundance in this compartment and that it is involved in the regulation of neuronal differentiation [202]. Nonetheless, it remains un-investigated how HOTAIRM1 responds to stress stimuli, specifically in ALS conditions.
With these premises, we first examined its behaviour in human iPSCs derived motor neurons (MNs) both WT and carrying the homozygous FUS^{P525L} mutation (from now on referred as HOMO MNs) [218], unperturbed and after oxidative stress induction through Sodium Arsenite ($NaAsO_2$) administration. To do that, we combined smFISH and immunofluorescence, respectively targeting HOTAIRM1, the stress granules marker G3BP1 and FUS. Looking at the smFISH, HOTAIRM1 signal is distributed both in the nucleus and in the cytoplasm (as previously reported in Rea et al., 2020 [202]), equally in WT and HOMO conditions (fig. 10A). Co-localization analysis, carried on with a custom macro in Fiji-ImageJ on both HOTAIRM1 and G3BP1 signals, showed that in stressed

WT MNs a substantial portion of HOTAIRM1 (64%) joins stress granules positive for G3BP1 (fig. 10A, upper panel and B), while WT FUS, as expected, mostly localizes in the nucleus (fig. 10A, upper panel). Moving on to HOMO MNs, where FUS de-localizes in the cytoplasm and participates in stress granules (fig. 10A lower panel), HOTAIRM1 is again recruited in stress granules as observed in WT, with 45% of spots co-localizing with SGs positive for both G3BP1 and FUSmut, 19% of signal co-localizing with G3BP1 alone and 4% co-localizing with FUSmut-only (fig. 10A lower panel and C). Put together, these data indicate that HOTAIRM1 is recruited in stress granules upon oxidative stress induction independently from FUS mutation. Indeed, as explained in Fig 10 B and C, both WT and HOMO MNs present the same percentage of HOTAIRM1 localized in SGs, with no-significant difference between the two conditions.
However, since HOTAIRM1 is constitutively recruited in stress granules, we wondered whether the lncRNA could have a role in the assembly and in the morphology of SGs. Indeed, in literature there are several examples of long non-coding RNAs that participate in the nucleation of SGs acting as a scaffold for RNPs [217], [219]. To test this hypothesis, we took advantage of iPSCs cells genetically engineered with a CRISPR/Cas9 approach [220] in order to knock-out HOTAIRM1 transcription. Then, we differentiated to MNs four different cell lines:

- WT/HOTAIRM1$^{+/+}$ iPSCs (WT);
- FUS^{P525L}/HOTAIRM1$^{+/+}$ iPSCs (HOMO);
- WT/HOTAIRM1$^{-/-}$ iPSCs (WT KO);
- FUS^{P525L}/HOTAIRM1$^{-/-}$ iPSCs (HOMO KO).

After differentiation and $NaAsO_2$ treatment, we then performed immunofluorescence against G3BP1 and FUS and evaluated particles size, number of particles per cell and co-localization percentage between FUS and G3BP1 particles, to determine if HOTAIRM1 could affect SGs formation. Importantly, since FUSmut does not always co-localize in SGs but can also form separate aggregates with different properties in composition and solubility [221]–[223], in HOMO MNs we independently analysed

G3BP1 signal, to determine SGs characteristics, and FUS signal, to determine FUSmut aggregates (FAs) features. Thus, thanks to the "analyse particles" function in Fiji-ImageJ, we looked at the average size of SGs and FAs and at the total number of particles per cell. Concerning the size of SGs (fig. 10D, left panel), we did not observe any difference among the samples when knocking out HOTAIRM1 or when comparing WT with HOMO samples, and the same observation applies to FAs in HOMO vs HOMO KO samples (fig. 10D, right panel). On the other hand, when looking at the number of particles per cell, a slight decrease in total number of SGs per cell (fig. 10E, left panel) in HOMO KO cells compared with HOMO MNs was detected, while no difference is observed in WT vs WT KO samples. Instead, when looking at the FAs number, the same trend, this time statistically significant, can be observed in HOMO vs HOMO KO (fig. 10E, right panel).
Finally, with a custom macro in Fiji-ImageJ, we also evaluated the percentage of co-localization between FUSmut and G3BP1 in HOMO samples, to test if HOTAIRM1 could perturb FUSmut ability to join SGs. Looking at the percentage of FUSmut associated with G3BP1 we did not observe any difference in the absence of the lncRNA HOTAIRM1 (fig. 10F), suggesting that HOTAIRM1 does not affect FUSmut' capacity to participate in SGs.

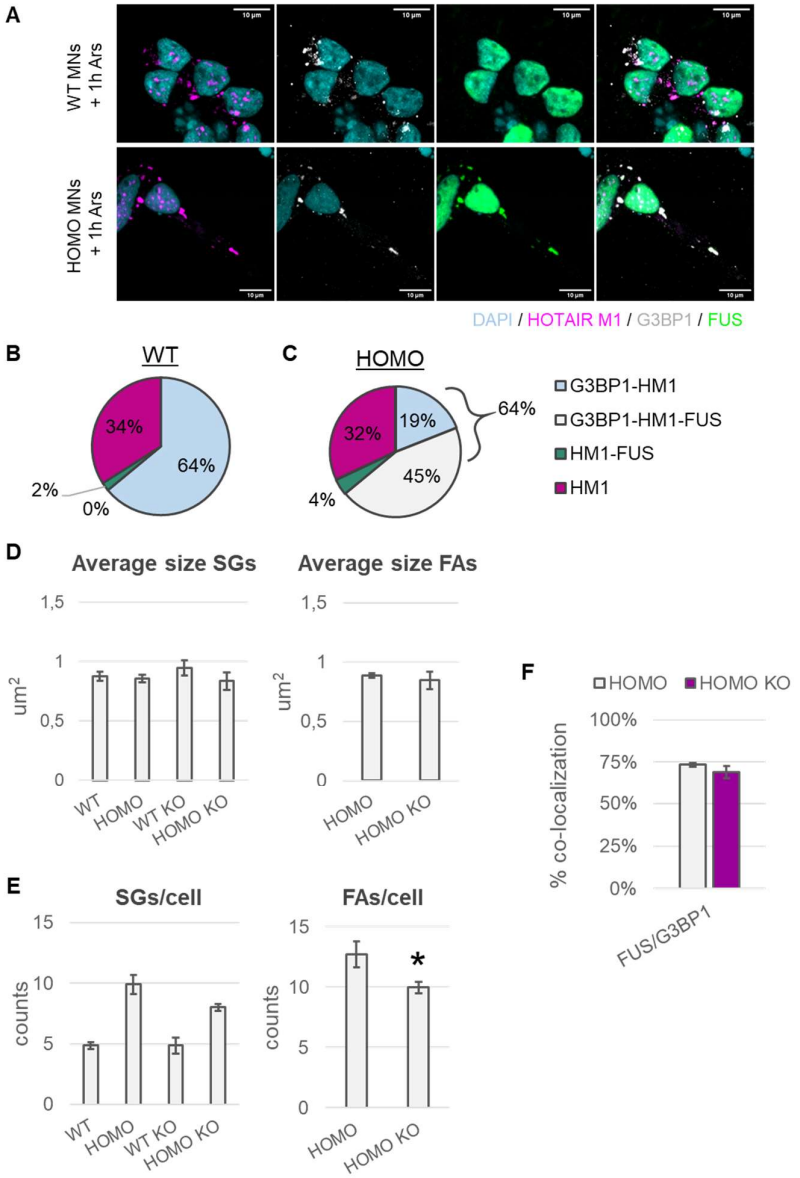
A
WT MNs + 1h Ars
HOMO MNs + 1h Ars
DAPI / HOTAIR M1 / G3BP1 / FUS
B
WT
34%
64%
2%
0%
C
HOMO
32%
19%
64%
45%
4%
G3BP1-HM1
G3BP1-HM1-FUS
HM1-FUS
HM1
D
Average size SGs
Average size FAs
um²
1,5
1
0,5
0
WT
HOMO
WT KO
HOMO KO
E
SGs/cell
FAs/cell
counts
15
10
5
0
*
F
HOMO
HOMO KO
% co-localization
100%
75%
50%
25%
0%
FUS/G3BP1

Figure 10: HOTAIRM1 co-localizes with stress granules and affects FUSmut aggregates formation.

A) *Combination of FISH and IF for the detection of HOTAIRM1 (magenta), G3BP1 (grey) and FUS (green) in stressed WT (upper panel WT MNs) or stressed ALS (lower panel) iPSCs derived motor neurons (HOMO MNs). Nuclei stained with DAPI are shown in cyan. Scale bars correspond to 10 μm.* ***B and C)*** *Pie charts representing HOTAIRM1 percentage of co-localization in WT (**B**) or HOMO (**C**) MNs with G3BP1-positive granules (light blue), FUSmut-positive granules (green), G3BP1- and FUSmut-positive granules (grey) and percentage of alone HOTAIRM1 spots (magenta). Mean percentages from 3 independent biological replicates are shown.* ***D)*** *Bar charts representing average size of SGs (left chart) in WT, HOMO, WT KO and HOMO KO MNs and of FAs (right chart) in HOMO and HOMO KO MNs. Error bars representing ± SEM (N=3).* ***E)*** *Bar charts representing number of SGs per cell (left chart) in WT, HOMO, WT KO and HOMO KO MNs and of FAs per cell (right chart) in HOMO and HOMO KO MNs. Error bars representing ± SEM (N=3).* ***F)*** *Bar charts showing percentage of co-localization between FUSmut and G3BP1 in HOMO and HOMO KO stressed MNs. Error bars representing ± SEM (N=3). ∗ $p < 0.05$ corresponds to an unpaired two-tailed.*

To summarize, we selected an interesting lncRNA, HOTAIRM1, focusing our investigation on its involvement in oxidative stress response. Indeed, combining FISH and IF assays we demonstrate its localization in stress granules in both WT and ALS MNs, suggesting that it might be recruited in SGs in order to preserve its cytoplasmic functions. In fact, examining the morphology and the number of SGs in WT motor neurons and in motor neurons knocked-out for HOTAIRM1, with the resolution limit imposed by a standard confocal microscope, we did not find any difference between the two samples, indicating that it might not have a role in the assembly of SGs. On the other hand, in ALS condition the depletion of HOTAIRM1 leads to a reduction in FUSmut aggregates, rising the hypothesis that the lncRNA, when bound to FUSmut, could enhance its aggregation properties.

Visualization of HOTAIRM1 throughout stress response in live mammalian cells

To further investigate HOTAIRM1 dynamics upon oxidative stress, also in this case, we decided to take advantage of the fRNA Pepper. In fact, live imaging of linear non-coding RNAs has been already achieved thanks to different fRNAs, including Pepper [1], [193], [196].
Therefore, we designed an over-expression construct to tag HOTAIRM1 with an array of 4xPepper inserted at the 3' end of the lncRNA (fig. 11A). Since we wanted to follow HOTAIRM1 behaviour during stress response, we transfected again HEK 293T cells stably expressing G3BP1 or FUSmut respectively tagged with GFP, as already done in the previous experiments. In figure 11B, over-expression efficiency of the engineered construct is shown in both HEK 293T lines, resulting in high transcript levels in both cell lines if compared with the housekeeping gene GAPDH. Importantly, the overexpression performance is much higher than the one of the circular RNAs previously tested (fig. 6C and D), making visualization of linear RNAs less demanding.
Hence, upon 24 hours of transfection, it was possible to visualize HOTAIRM1 bound to HBC620 dye: as expected from the overexpression efficiency, a nice proportion of the total transfected cells provided a good fluorescent signal, mostly diffused in the cytoplasm (fig. 11C and E).
Transfecting HOTAIRM1 tagged with Pepper in G3BP1-GFP HEK cells, it was possible to observe its behaviour throughout the whole stress event. Since the oxidative stress response is an acute event that could compromise the viability of the cells, we performed live imaging from the moment of its induction with a temporal resolution of 1 minute per frame, to avoid excessive perturbation of cells.
As expected, within the first 30 minutes upon $NaAsO_2$ treatment, we witnessed liquid-liquid phase separation of G3BP1, forming droplet-like structures that will become SGs (fig. 11C). Interestingly, as shown in the magnified detail in figure 11D,

corresponding to the same timing of G3BP1 LLPS, also HOTAIRM1 undergoes a condensation event. Importantly, HOTAIRM1 condensation is independent from the G3BP1 one (fig. 11D upper panel), indeed only during the process of LLPS it is possible to observe the merge of both the ncRNA and the protein participating in the mature SG structure (fig. 11D lower panel).

This intriguing observation made us speculate that some other protein that partakes in SGs and is able to undergo LLPS, could mediate HOTAIRM1 recruitment. Therefore, as we already determined that HOTAIRM1 interacts with FUS [202] and that co-localizes with SGs containing FUSmut (fig. 10A and B), we performed the same experiment in HEK 293T cells expressing FUSmut-GFP, to establish if HOTAIRM1 joins and contributes to FUSmut' LLPS. As shown in figure 11E, upon stress induction, also FUSmut condensates in droplet-like structures, as well as HOTAIRM1. Unexpectedly, looking at how the signals of HBC and GFP interplay (fig. 11F), we observed the same dynamic depicted between HOTAIRM1 and G3BP1, with disjointed condensation events, that come together in later time points of the oxidative stress response.

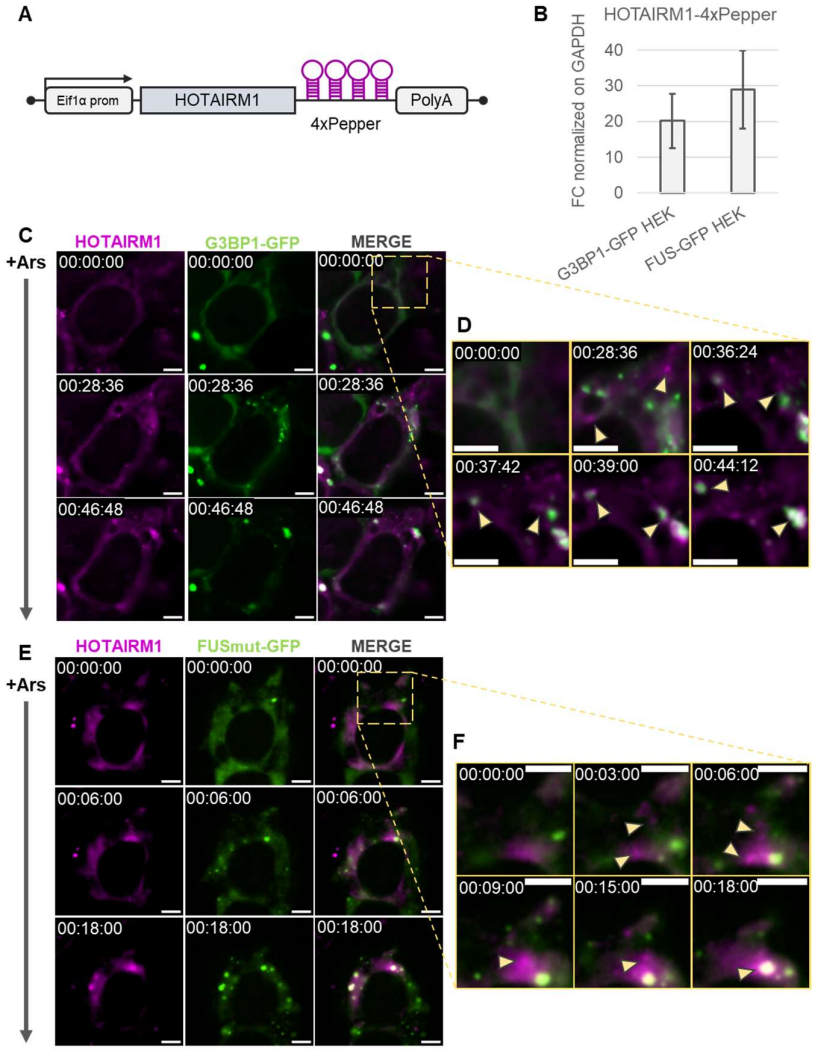

Figure 11: HOTAIRM1 undergoes independent LLPS before being recruited in WT or ALS-like granules.

A) Schematic representation of the engineered construct for the over-expression of HOTAIRM1 tagged with an array of 4xPepper at its 3' terminus. B) Expression levels of HOTAIRM1-4xPepper normalized on the one of GAPDH, quantified by

qPCR in G3BP1-GFP stable HEK 293T and in FUSmut-GFP stable HEK 293T. Error bars representing ± SEM (N=3). ***C)*** *Representative cells (N=2 biological replicates) imaged with a wide-field microscope expressing both HOTAIRM1 labelled with HBC 620 fluorogenic dye (magenta) and G3BP1-GFP (green). Time 00:00:00 corresponds to 0.5 mM $NaAsO_2$ administration (upper row), while in following time points (second and third row) formation of stress granules can be followed (duration 1h; interval ~1min).* ***D)*** *Magnification view of cell in panel* ***C*** *showing HOTAIRM1 and G3BP1 first undergoing independent LLPS throughout the oxidative stress event and finally merging (time point 00:39:00 and 00:44:12).* ***E)*** *Representative cells (N=2 biological replicates) expressing both HOTAIRM1 labelled with HBC 620 fluorogenic dye (magenta) and FUSmut-GFP (green). Time 00:00:00 corresponds to 0.5 mM $NaAsO_2$ administration (upper row), while in following time points (second and third row) formation of FUSmut condensates can be followed (duration 1h; interval ~1min).* ***F)*** *Magnification view of cell in panel* ***E*** *showing HOTAIRM1 and FUSmut first undergoing independent LLPS throughout the oxidative stress event and finally merging (time point 00:18:00). All scale bars correspond to 5 μm.*

To strengthen our observations, we also performed higher temporal resolutions acquisitions to perform single particle tracking: imaging already stressed cells for 15 minutes with ~11 seconds per frame, we were able to capture and track HOTAIRM1 stably but dynamically interacting with G3BP1 (fig. 12A and B), while independent HOTAIRM1 spot joins the pre-formed stress granule (fig. 12A, middle row and 12B).

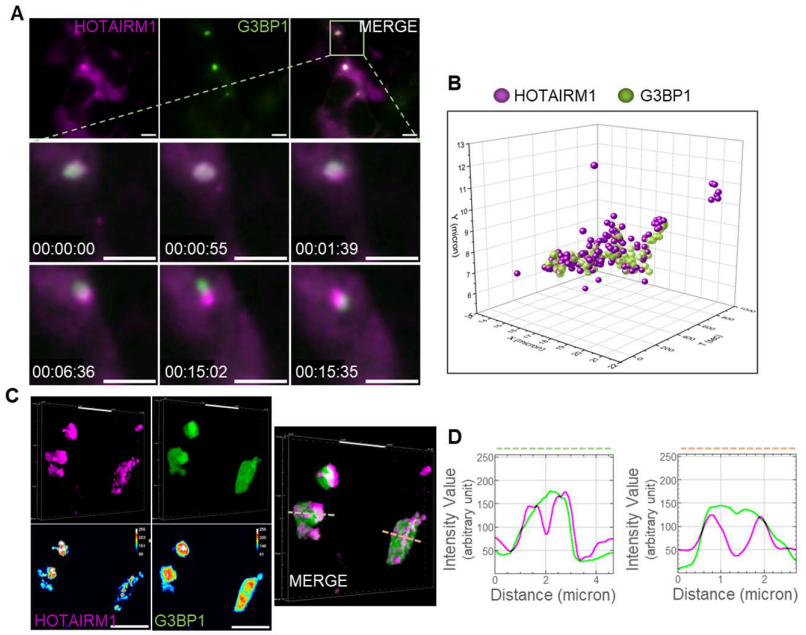

Figure 12. Exogenous HOTAIRM1 joins G3BP1-GFP tagged SGs in HEK 293T cells.

__A)__ Representative cells (N=2 biological replicates) imaged with a wide-field microscope expressing both HOTAIRM1 labelled with HBC 620 fluorogenic dye (magenta) and G3BP1-GFP (green). Lower panel shows a magnification view of HOTAIRM1 and G3BP1 particles interacting over time (duration 15min; interval ~11sec). __B)__ Single particle tracking of HOTAIRM1 and G3BP1 over time. The plot indicates HOTAIRM1 (magenta) and G3BP1 (green) xy-coordinates (micron) as a function of time (sec). __C)__ 3D rendering of two representative SGs containing HOTAIRM1 (magenta) and G3BP1 (green) imaged with 3D-SIM. Lower panels represent intensity map showing relative gray scale intensities of Z-projections. __D)__ Intensity value (arbitrary unit) of HOTAIRM1 (magenta) and G3BP1 (green) showing their signal distribution along a reference line crossing a representative SG. All scale bars correspond to 5 µm.

A symmetrical observation was made on FUSmut condensates (fig. 13A and B), suggesting that LLPS of HOTAIRM1 upon stress induction is not driven by FUSmut, even if in the cytoplasm they are known to directly bind each other [202].

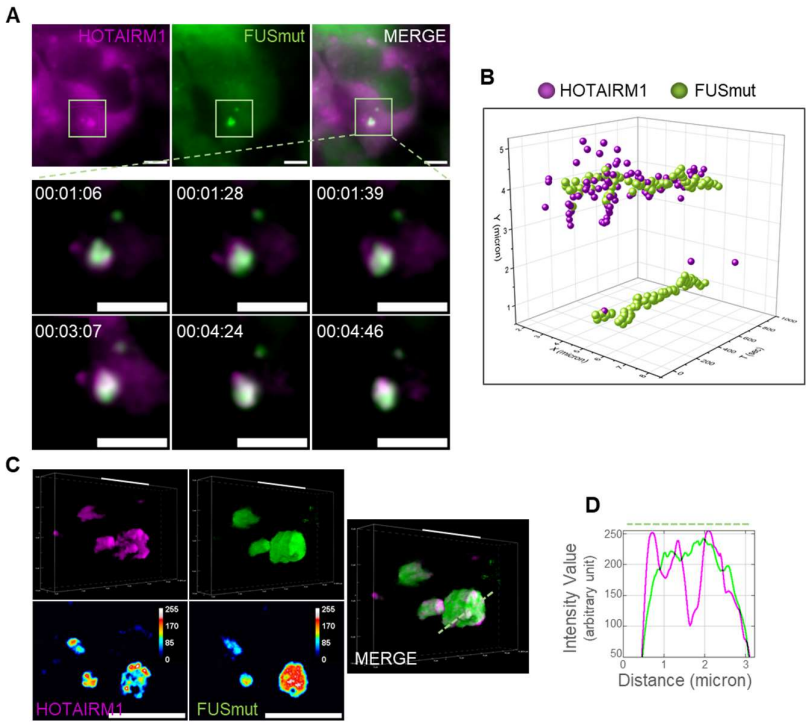

Figure 13: Exogenous HOTAIRM1 joins FUSmut-GFP tagged aggregates in HEK 293T cells.

A) *Representative cells (N=2 biological replicates) imaged with a wide-field microscope expressing both HOTAIRM1 labelled with HBC 620 fluorogenic dye (magenta) and FUSmut-GFP (green). Lower panel shows a magnification view of HOTAIRM1 and FUSmut-GFP particles interacting over time (duration 15min; interval ~11sec).* ***B)*** *Single particle tracking of HOTAIRM1 and FUSmut-GFP over time. The plot indicates HOTAIRM1 (magenta) and FUSmut (green) xy-coordinates (micron) as a function of time (sec).* ***C)*** *3D rendering of two representative aggregates containing HOTAIRM1 (magenta) and FUSmut (green) imaged with 3D-SIM. Lower panels represent intensity map showing relative gray scale intensities of Z-projections.* ***D)*** *Intensity value (arbitrary unit) of HOTAIRM1 (magenta) and FUSmut (green) showing their signal distribution along a reference line crossing a representative SG. All scale bars correspond to 5 µm.*

Moreover, also in the case of HOTAIRM1 we performed SIM on the granules in which it is recruited, to determine its sub-structural distribution. In figures 12C and 13C respectively, G3BP1 granules and FUSmut condensates containing HOTAIRM1 were analysed: intensity maps (fig. 12C and 13C, lower panel) and signal profile plots (fig. 12D and 13D) revealed that HOTAIRM1 is characterized by an uneven signal distribution with multiple focal points, that preferentially localize in the shell of the granules, both in the case of G3BP1 and FUSmut. This signal distribution is quite distinguishable from the one of the two proteins, which show a uniform pattern, with the highest intensity peaks in the core of the structures.

Hence, thanks to the fRNA Pepper, we were able to follow HOTAIRM1 lncRNA dynamics throughout the oxidative stress response. Importantly, we were able to add stimulating observations to what we already determined with experiments on fixed motor neurons. Indeed, in fixed cells, we evaluated HOTAIRM1 co-localization with physiological and pathological stress condensates, but, thanks to live imaging assays, we were able to determine that the early events of HOTAIRM1 condensations are mediated by neither G3BP1 nor FUSmut, and that, therefore, a third party protein or a distinct RNP is responsible for the recruitment of HOTAIRM1 in stress granules.

6. DISCUSSION

Many technologies to perform live imaging of mRNAs are widely used to follow most of the steps of their metabolism, including nuclear export, transport and translation, [148], [149], [179], [187]; nonetheless, just a few examples are provided in literature to image non-coding RNAs in live cells, as they are often low abundant, short and highly structured molecules. Especially when it comes to circRNAs, their detection can be quite challenging, as they share their whole sequence with their linear counterparts, but the back-splicing junction, the unique region that allows distinguishing them.

In this work, we put our effort in designing a strategy for imaging of circular RNAs in live mammalian cells, in order to delve into the dynamics of the ALS-related circular RNAs circ-16 and circ-31, and more in general to provide a tool for an all-encompassing visualization of circRNAs. To do that, we exploited the newly described fRNA Pepper [1], generating and characterizing over-expression constructs of our circRNAs of interest tagged with it.

Before imaging, we evaluated circularization efficiency and proper localization of the exogenous circRNAs, to assess Pepper fRNA impact on circRNAs over-expression. Importantly, Pepper fRNA does not impair the proper localization of the circRNA. However, depending on the length of the circular RNA sequence, on the length of the ICSs and possibly on the number of Pepper arrays, the fRNA tag could impede proper circularization of the exogenous transcript, making the selection of the candidate circRNA and of the insertion site crucial for its visualization. Indeed, we pointed out some critical steps in tagging circular RNAs, as differences in the length of the target, in the number of Pepper arrays and in the insertion sites provided completely different yields of the over-expression constructs, requiring a more demanding design, depending on the circular RNA. In fact, we found that the over-expression constructs

designed for circ-16 needs further optimization before employing it for imaging purposes.

Nonetheless, we successfully imaged circ-31 in live HEK 293T cells, determining its participation in G3BP1 and FUSmut positive RNPs, possibly recapitulating the mechanism though which it shuttles along axons in motor neurons, the cells in which it is more expressed. Importantly, this would provide the first example of a circular RNA detected with a fluorescent RNA and with a technology compatible with a super-resolution technique [174], opening important scenarios on the study of the dynamics and the sub-cellular localization of such RNA species.
Notably, circ-31 loading in G3BP1 and FUSmut positive RNPs adds a novel layer, while rising key questions, on the understanding of the mechanism through which it is recruited in stress granules, and more importantly in pathological ALS aggregates [2]. Therefore, future experiments will be definitely aimed at observing its behaviour upon oxidative stress trigger, with a special consideration for its interaction with P-bodies, which might unveil novel information about its functions and its metabolism.
Intriguingly, experiments performed in our laboratory also demonstrated that circ-31 also owns some interactions sites for several messenger RNAs, including transcripts of centrosome-associated protein (Sdccag8) [224], translation initiation factor subunits (Eif3C and Eif4g3) [225] and interestingly, Vps53 and Rufy1, both encoding for proteins involved in vesicle trafficking [226], [227] (data not shown). As circRNAs are known to work as scaffolds for proteins and mRNAs transport, it will be interesting, in the future, to assess whether these mRNAs participate in the interaction between circ-31 and PBs, possibly determining one of the functions of our circular RNA of interest. To do that, we are currently planning to combine smFISH and IF to target circ-31, the mRNAs and DCP1A protein.

Furthermore, committed to find novel mechanism through which non-coding RNAs contribute to LLPS-based processes, we also determined the co-localization of the long non-coding RNA HOTAIRM1 with physiological and pathological stress granules in human iPSCs-derived motor neurons. Importantly, approaching these questions with imaging procedures was mandatory: its inclusion in SGs has in fact eluded all transcriptomic data available in literature, as none of the SGs purification protocols was conducted in mature mammalian neurons [216], [217], [228].

In addition, we took advantage of the fRNA Pepper to follow its dynamics during the oxidative stress response in HEK 293T cells, surprisingly observing that in the early stages of the process HOTAIRM1 undergoes LLPS that is neither mediated by G3BP1. Nonetheless, even if we observed the same independent LLPS of HOTAIRM1 and FUSmut, biochemical interaction assays pointed out that the lncRNA interacts with FUS in unperturbed conditions, requiring supporting experiments to conciliate these two observations. Interestingly, another protein that is known to interact with HOTAIRM1 is Annexin A11 [202], a protein found in SGs and recently described to be able to phase-separate and to be involved in long-distance transport of RNA granules [229]. It could hence provide a suggestive candidate to further explore the dynamics of HOTAIRM1 recruitment in SGs.
Finally, analysing the morphology of SGs in both fixed and live samples, and taking advantage of super-resolved SIM, we were able to conclude that HOTAIRM1 does not participate in the formation of the core of SGs, but it is preferentially recruited in their shell.
Importantly, these observations are in line with the interpretation given to the experiments performed in fixed motor neurons, where no changes in stress granules morphology upon HOTAIRM1 knock-out lead us to speculate that he does not participates in any critical step of SGs assembly. However, we hypothesized its possible involvement in FUSmut aggregation, as evaluating FAs formation

in the absence of the lncRNA we witnessed a significant reduction in number of FUSmut aggregates per cell.

Overall, fRNA Pepper, allowed us to image two distinct species of non-coding RNAs, circular RNAs and long non-coding RNAs, representing a powerful tool to study their dynamics in relationship with RNPs transport and neurodegeneration-linked processes.
While it proved very effective to image a linear RNA, efficiency for the circular RNAs, in terms of number of positive cells, signal-to-noise ratio and transcript specificity, can be certainly improved.
In fact, one of the major limitations encountered has been the inability to image cells with a good signal-to-noise ratio for circ-31 fluorescence, but at the same time with a non-condensed state of G3BP1 or FUSmut. This suggested us that the over-expression performance of the p-circ construct does not provide an optimal yield in fluorescent signal, unless the RNA is compartmentalized, creating specific foci.

Importantly, this technique is designed to image exclusively exogenous RNAs, providing a complementary tool to collect supplementary information about RNAs localization, interactome, and dynamics, but that needs to be coupled with experiments in fixed samples to focus on the endogenous species. Moreover, we found the efficiency of the technique to be directly proportional to the transfection efficiency, making quite challenging to image RNAs in more complex cellular systems such as post-mitotic differentiated neurons, which are known to not respond well to transfection agents. However, when studying very abundant long non-coding RNAs, a suggestive option could be tagging the endogenous transcript with the fRNA through genome editing techniques, such as CRISPR/Cas9.

Notably, in the meanwhile, other fluorescent RNAs have been developed, that match Pepper's efficiency if not overcome it, providing a wider palette in the selection of the fRNA depending on

the target complexity. Jäschke and colleagues can give an example, as they developed the fRNA RhoBAST [230], a novel rhodamine-binding aptamer compatible with super-resolved single-molecule localization microscopy (SMLM).
Intriguingly, a few months ago also inert Pepper (iPepper) was engineered [231], a novel version of Pepper designed to target endogenous mRNAs, opening new perspectives in the study of both translating and non-coding RNAs species in more advanced cellular systems and eliminating the biases that might be given by over-expression experiments.

7. MATERIALS AND METHODS

7.1 Plasmid construction

To produce the p-circ31 and p-circ16 plasmid series the described steps were followed: a doxycycline-inducible backbone endowed with flanking inverted complementary sequences (ICSs) [39], [62] for enhanced overexpression of the circular RNAs was already present in the lab. Starting from this plasmid, the In-Fusion HD Cloning kit (Takara Bio) was used to replace the sequence for puromycin resistance with the sequence of the Blue Fluorescent Protein (tagBFP), amplified from the Addgene plasmid (#55312). The SV40 nuclear localization sequence (CACTTTCCGCTTTTTCTTTGG, Addgene plasmid #39319) was cloned downstream the tagBFP combining inverse PCR and ligation of blunt ends (T4 Ligase NEB). The sequences of both circ-Hdgfrp3 (exons 2-3-4-5) and circ-Dlc1 (exon 2) were PCR-amplified form SK-N-BE cells cDNA and cloned between the ICSs using In-fusion Cloning Kit (Takara Bio). 4xPepper array sequence was amplified from the pAPU6-MCS-Pepper (PAPU604MCS1 FR Biotechnology©) plasmid and cloned within exon 4 (base 43-44) and exon 5 (base 71-72) of the circ-Hdgfrp3 sequence by In-Fusion Cloning Kit (Takara Bio) to obtain the final constructs p-circ31_s1 and p-circ31_s2. Similarly, for p-circ16_s1 and p-circ16_s2 the sequence for 8xPepper was amplified from the pcDNA 3.1 (-) – 8xPepper plasmid (Genescript), and inserted with In-Fusion Cloning Kit (Takara Bio) between base 785-786 and between base 989-990 of Dlc1 exon 2.
The sequence of HOTAIRM1 tagged with 4xPepper was instead cloned in an ePB-bsd-Eif1a (PiggyBac transposable vector) backbone [232] using sequential In-Fusion Cloning (Takara Bio) reactions. The same strategy was used to generate the plasmids expressing the proteins G3BP1, FUS and DCP1A tagged with eGFP. CloneAmp HiFi PCR Premix (Clontech) was used for all the PCR amplifications.

7.2 Cell culture

Thawing and amplification of HEK 293T cells

HEK 293T cells stored at -80°C in freezing medium (DMEM high glucose Sigma® supplemented with 20% FBS Gibco and 10% DMSO), were quickly defrosted at 37°C, using a thermostatic bath. After removing the freezing medium by centrifugation (5 min at 1000 rpm), cells were resuspended in the appropriate amount of maintaining medium (DMEM high glucose Sigma® supplemented with 10% FBS, 2 mM GlutaMAX Sigma® and 1% Penicillin/Streptomycin Sigma®) and plated to allow maintenance and amplification. For live imaging experiments the common DMEM high glucose Sigma® was replaced with FluoroBrite™ DMEM (Thermo Fisher).

Selection of HEK 293T stable cell lines

To produce HEK 293T cell lines stabling expressing G3BP1-GFP, GFP-FUSmut and GFP-DCP1A, 2.5 x 10^5 cells were plated on 6 cm dishes. The next day cells were transfected with a solution of Optimem (Thermo Fisher), 5 µg of specific plasmid, 0.5 µg of hybrid transposase plasmid and Lipofectamine 2000 transfection reagent (Invitrogen™) with a 1:2.5 DNA:transfection reagent ratio.

Cell transfection and induction

For live imaging experiments, 1,5 x 10^4 HEK 293T cells per well were plated two days before transfection in 8-well Nunc™ Lab-Tek™ II Chambered Coverglass, previously coated with Geltrex (Thermofisher Scientific) incubated at 37°C for at least 3 hours. Similarly, for expression and circularization efficiency experiments, 2 x 10^4 HEK 293T cells were plated two days before transfection on 12-multiwell plate (Corning) coated with 500 µl of Attachment factor X (Gibco) and incubated for 30 min at room temperature. For

nucleus-cytoplasm fractionation experiments, 3.5 x 10^5 cells were instead plated on 6 cm dish (Corning), always two days before transfection.
In both live imaging and circularization efficiency experiments, cells were transfected using a solution of Optimem (Thermo Fisher), 1:2 DNA:FuGENE® HD transfection reagent (Promega) ratio and 2 μg of specific plasmid, while in the case of nucleus-cytoplasm fractionation experiment the amount of selected plasmid was 2 μg/ml. In case of circular RNAs overexpression experiments, circRNAs transcription was induced using doxycycline at a final concentration of 2 μg/ml, the day after transfection.

Differentiation of induced Pluripotent Stem cells (iPSCs)-derived Motor Neurons

Human iPSCs were maintained and differentiated in spinal motor neurons as described in De Santis et al., 2018 [218]. Briefly, iPSCs were dissociated to single cells with Accutase (Thermo Fisher Scientific) and plated in Nutristem-XF/FF medium (Biological Industries) supplemented with 10 μM ROCK inhibitor (Enzo Life Sciences) on Matrigel (BD Biosciences) at a density of 100′000 cells/cm^2. The day after, differentiation was induced by adding 1 μg/ml doxycycline (dox) (Thermo Fisher Scientific) in Nutristem without bFGF and TGFβ (Biological Industries) in order to drive the expression of NIL (Ngn2-F2A-Isl1-T2A-Lhx3) plasmid. After 48 hours of dox induction, medium was changed to Neurobasal/B27 medium (Neurobasal Medium, Thermo Fisher Scientific, supplemented with 1X B27, Thermo Fisher Scientific, 1X Glutamax, Thermo Fisher Scientific, 1X NEAA, Thermo Fisher Scientific, and 0.5X Penicillin/Streptomycin, Sigma Aldrich), containing 5 μM DAPT and 4 μM SU5402 (both from Sigma Aldrich). At day 5, cells were dissociated with Accutase (Thermo Fisher Scientific) and plated on Matrigel (BD Biosciences) coated dishes. 10 μM ROCK inhibitor was added for the first 24 hours after dissociation. Neuronal cultures were maintained in neuronal

medium (Neurobasal/B27 medium supplemented with 20 ng/ml BDNF, 10 ng/ml GDNF, both from PeproTech, and 200 ng/ml l-ascorbic acid, Sigma Aldrich).
For experiments carried out in stress condition, Sodium Arsenite ($NaAsO_2$) at a final concentration of 0.5 mM was added to the neuronal medium and incubated for 1 hour.

7.3 Nucleus-Cytoplasm fractionation

Nucleus-Cytoplasm fractionation was performed as described in Conrad and Ørom, 2017 [233] to evaluate the subcellular localization of the circular and the linear precursor isoforms transcribed from p-circ over-expression constructs.
All centrifugation steps were carried out at 4°C and all buffers were ice cold.
Briefly, HEK 293T cells, previously transfected and induced as indicated above, were detached adding 0.5 ml of 0.25 % Trypsin solution (Gibco) and incubating at 37°C for 5 min and the trypsinization reaction was then inactivated adding 1.5 ml of HEK maintaining media. Cell suspension was transferred into a 15 ml falcon tube, spun for 5 min at 200 × g in a tabletop centrifuge and the supernatant was aspirated. Cell pellet was resuspended in 10 ml PBS and spun at 200 × g for 5 min. The supernatant was removed, cell pellet was resuspended in 1 ml PBS and transferred to a 1.5 ml Eppendorf tube, spun at 200 × g in a microcentrifuge for 2 min and the supernatant was carefully removed again. 400 µl of Igepal lysis buffer (10 mM Tris pH 7.4, 150 mM NaCl, 0.15 % Igepal CA-630) was added to the pellet, gently pipetted up and down 3–5 times to resuspend the cells, and the solution was incubated in ice for 5 min. The cell lysate was gently transferred in a new Eppendorf and overlayed on top of a 1 ml sucrose buffer (10 mM Tris pH 7.4, 150 mM NaCl, 24 % sucrose) by slowly pipetting to the wall of the tube. The solution was centrifuged at 3500 × g for 10 min and the supernatant, containing the cytoplasmic fraction, was transferred in

another tube and cleared again by centrifugation 14,000 × g for 1 min. Instead, the pellet obtained after the centrifugation in sucrose buffer, corresponded to the nuclear fraction, was resuspended in TRIZOL (Thermo Fisher). RNA was extracted and analysed as indicated below.

7.4 Live imaging of Pepper-tagged RNAs

HEK 293T cells, previously transfected and induced as indicated above, were incubated for 5-30 minutes in medium supplemented with $MgSO_4$ 5 mM and HBC620 0.5 µM (FR biotechnology™) following manufacturer instructions. For experiments carried out in stress condition, $NaAsO_2$ at a final concentration of 0.5 mM was added to the imaging medium and incubated for 1 hour after HBC treatment to visualise RNAs during oxidative stress response.

7.5 RNA analysis

RNA extraction and reverse transcription

To evaluate overexpression and circularization efficiency and to assess exogenous RNA sub-cellular localization, RNA was extracted using Direct-zol RNA mini-prep kit (Zymo research) following manufacturer instructions 48 hours after transfection of over-expression constructs. For nucleus-cytoplasm fractionation experiments, RNA was extracted from the whole nuclear fraction and from 1/7 of the total cytoplasmic fraction. Residual genomic and plasmidic DNA was removed using DNA-free kit (Invitrogen™) and 500 ng of RNA were retro-transcribed with PrimeScript RT Master Mix (Takara Bio) following manufacturer instructions. For nucleus-cytoplasm fractionation experiments, an iso-volumetric amount of RNA up to 500 ng was retro-transcribed from the two fractions.

qPCR

cDNA obtained from retro-transcription was analysed by qPCR using the PowerUp SYBR Green Master Mix (Thermo Fischer) reagent coupled with a Quant-Studio 5 (Applied Biosystems) machine. For each reaction 5 ng of cDNA, 7.5 µl of SYBR Green, 0.5 µl of forward primer (330 µM as final concentration), 0.5 µl of reverse primer (330 µM as final concentration) and ddH_2O up to 15 µl of total reaction volume were used. Three technical replicates for each selected target were analysed on plate 96 well 0.1 ml (Applied Biosystems™, 4346906).
For over-expression and circularization efficiency experiments, analysis of qPCR data was conducted as follow: first, the Delta Ct between the target RNA and the reference gene GAPDH was calculated. Those values were then used to calculate the Fold change (FC), so the relative expression of the specific RNA isoform compared to a housekeeping gene. The FC of three independent biological replicates was used to calculate the average FC, the standard deviation (SD) and the standard error (SE), shown in the error bars. As statistical test able to assess the statistical significance of the divergence between different samples the unpaired, two-tailed Student's T test was chosen. For qPCR performed for nucleus-cytoplasm fractionation experiments, the logarithm to the base of 7 of 2 was subtracted to all the Ct means of the cytoplasmic fractions, to account for dilution coefficient. Then, the sum between nuclear and cytoplasmic (adjusted) Cts was calculated and used as reference to calculate the relative percentage of transcript in the specific compartment.

7.6 Fluorescent *in situ* Hybridization and Immunofluorescence

iPSCs derived Motor Neurons were plated on 12 mm diameter coverslips coated with Geltrex (Thermofisher Scientific) and fixed

in 4% paraformaldehyde (Electron Microscopy Sciences, Hatfield, PA) for 10 min at room temperature. Dehydration step with ice-cold Ethanol series (50%, 70%, 100%) was performed in order to store cells at -20°C in absolute ethanol until use.
HOTAIRM1 was detected via Fluorescent *in situ* Hybridization (FISH) with a mix of 18 biotinylated probes (Sigma) as described in Santini, Martone, Ballarino 2021 and in Vautrout et al., 2015 [171], [172]. Briefly, iPSCs derived motor neurons were rehydrated by descendent ice-cold ethanol series (100%, 70%, 50%) and permeabilized in a solution of 0.05% Triton X-100 and 2 mM VRC (Sigma-Aldrich, R3380) in DPBS for 5 min. Cells were then washed three times in DPBS before replacing with 2X SSC buffer (3 M NaCl; 0.3 M sodium citrate in nuclease free water for a 20X stock solution). 5 min incubation in SSC was followed by incubation with pre-hybridization buffer (10% deionized formamide, Sigma-Aldrich, 47671; 2X SSC in nuclease free water) for 15 min at 37°C. Motor neurons were then incubated over night at 37°C in a slide hybridizer machine (ACD HybEZ™ II Hybridization System) with hybridization buffer (10% deionized formamide; 2X SSC; 10% w/v Dextran sulfate, Sigma-Aldrich, D8906, 2 mM vanadyl ribonucleoside complexes (VRC), Sigma-Aldrich, R3380, in nuclease free water) completed with the biotinylated probes at a final concentration of 50 nM each. The next day cells were washed twice with 2X SSC for 5 min first at 37°C and then at RT. SSC buffer was then discarded and coverslips were incubated with TN buffer (Tris HCl pH 7.5 10 mM; NaCl 5 mM in nuclease free water) at RT for 10 min. Finally, biotinylated oligoes were stained incubating with 1:200 diluted Alexa Fluor™ 568-conjugated streptavidin (Invitrogen™ S11226) in 4% w/v BSA (Sigma-Aldrich, A2153)/TN buffer for 1-2 hours at RT in a humid box.
When FISH staining was combined with Immunofluorescence (IF), or to perform IF alone, cells were washed twice with TN buffer (only when coupling FISH with IF) and once with DPBS for 5 min at room temperature and then were incubated with primary antibodies (anti-FUS produced in rabbit, Bioss Antibodies bs-2980R, anti-FUS

produced in mouse, Santa Cruz sc-47711, anti-G3BP1 produced in chicken, Sigma GW22382A, anti-G3BP1 produced in rabbit, Sigma PLA0231) diluted in 1% w/v BSA/DPBS for 1 hour at room temperature. Subsequently, samples were washed three times with DPBS for 5 min at room temperature and incubated with 1:300 diluted secondary antibodies (Goat anti-Mouse Alexa Fluor™ 488, Invitrogen A-11029; Goat anti-rabbit Alexa Fluor™ 488, Invitrogen A-11008; Donkey anti-Rabbit Alexa Fluor™ 594, Immunological Sciences IS-20152-1, Goat anti-Chicken Alexa Fluor™ Plus 488, Invitrogen A32931) in 1% w/v BSA/DPBS for 45 min at room temperature. Lastly, cells were washed three times with DPBS for 5 min at room temperature, nuclei were counterstained with DAPI solution (Sigma, D9542; 1ug/ml/PBS) for 5 min at room temperature and coverslips were mounted with Prolong Diamond Mounting Media (ThermoFischer Scientific, P-36961).

7.7 Image acquisition

Fixed samples were imaged on a Nikon Instrument A1 Confocal Laser Microscope equipped with a 1.49 NA 100x objective (Apo TIRF 100x Oil, Nikon, Tokyo, Japan). Confocal images were collected with NIS-Elements AR software (Nikon): ND Acquisition module was used for multipoint acquisition of Z-stack images (150-175nm Z-spacing) of 4 um thickness.
All live imaging experiments were performed using an Eclipse Ti2-E Inverted Microscope equipped with the Nikon Super Resolution System (N-STORM & N-SIM), with a 1.49 NA 100x objective (Apo TIRF 100x Oil, Nikon, Tokyo, Japan) and with a 3D EX V-R 100x/1.49 Grating Block. SIM images were collected with NIS-Elements AR software (Nikon): ND acquisition module was used for Z-stack (150-180nm Z-spacing) images collection and for time-lapse acquisition. Specifically, time-lapses with duration of 15 min and “no delay” (~11 sec) interval were collected for higher temporal resolution acquisitions and time-lapses with duration of 1hour and 1

or 3 minutes interval were collected for lower temporal resolution acquisitions. The three reconstruction parameters illumination modulation contrast, high-resolution noise suppression and out of focus blur suppression were adopted to generate consistent Fourier transform. Images with a reconstruction score of 8 were selected for sub-structural analysis.
Occasionally, the Denoise.ai and the Clarify.ai deconvolution algorithms available on NIS-Elements AR software (Nikon), were used to post-process widefield time-lapse acquisitions.

7.8 Co-localization analysis and particles measurements on fixed samples

Fiji-ImageJ open source software was used for semi-automated analysis on confocal images of immunofluorescence and FISH experiments using custom macros.
Briefly, count and measurements on stress granules and FUSmut aggregates were performed on Z-projections of confocal images thanks to the "Analyze particles" function. Moments thresholding algorithm was used to make images binary and total number and average size of particles > 0.05 μm was calculated. Number of particles per cell was then obtained as a ratio of total amount of particles per number of nuclei, stained with DAPI.
For object-based co-localization analysis between the lncRNA HOTAIRM1, G3BP1 and FUSmut or between G3BP1 and FUSmut only, Moments algorithm was exploited again to create binary masks for every acquisition channels. The Image Calculator command was then used to subtract nuclei masks to HOTAIRM1, G3BP1 and FUSmut channels in order to account only for cytoplasmic signal. To detect co-localizing particles in the cytoplasm, the Image Calculator "AND" function was then applied to create secondary masks resulting from the intersection of the pixels between: HOTAIRM1 and G3BP1; HOTAIRM1 and FUSmut; HOTAIRM1, G3BP1 and FUSmut or between FUSmut

and G3BP1. “Analyze particles” function was again used to count number of total particles and number of particles in the intersection masks, thus percentages of co-localization were obtained as a ratio between particles in the intersection mask/total number of particles. Co-localization analysis and particles measurements were all performed on three independent biological samples. Statistical significance of the variance between different biological conditions was calculated with the unpaired two-tailed Student's t-test.

7.9 Single-particle tracking and sub- structural distribution of ncRNAs and RNPs in live cells

TrackMate plug-in was used for single-particle tracking of Pepper-tagged RNAs interacting with G3BP1-, FUSmut- or DCP1A-GFP [206], [207]. Representative Regions-of-interest (ROIs) were selected from time-lapse acquisition with duration of 15 min and “no delay” (~11 sec) interval, collected with widefield microscopy. DoG Detector algorithm was selected and an “estimated object diameter” of 1 μm was chosen to filter for the objects to track, while “Quality threshold” was determined case by case. Simple Linear Assignment Problem (LAP) tracking algorithm [234] was then exploited with the following configuration options:

- Linking max distance: 5 μm;
- Gap-closing max distance: 5 μm;
- Gap-closing max frame gap: 3.

Finally, “track tables” recording single spots IDs and xy-coordinates frame-by-frame were extrapolated and used to generate 3D scatter plots with the Origin software. In particular, x-axis was assigned to x-coordinates, y-axis was assigned to time position and z-axis was assigned to y-coordinates.

The “volume view” function of NIS-Elements AR software (Nikon) was exploited for 3D rendering of signals of Pepper-tagged RNAs and GFP-tagged proteins acquired with SIM. Intensity maps for

qualitative examination of the signal distribution of Pepper-tagged RNAs and GFP-tagged proteins were generated applying the “royal” LUT (Look Up Table) available in Fiji-Image, while profiles of the signal distribution were generated along an arbitrary line with the function “Analyze > Plot Profile” of the Fiji-ImageJ menu.

8. BIBLIOGRAPHY

[1] X. Chen *et al.*, 'Visualizing RNA dynamics in live cells with bright and stable fluorescent RNAs', *Nat Biotechnol*, vol. 37, no. 11, pp. 1287–1293, Nov. 2019, doi: 10.1038/s41587-019-0249-1.

[2] E. D'Ambra *et al.*, 'Circ-Hdgfrp3 shuttles along neurites and is trapped in aggregates formed by ALS-associated mutant FUS', *iScience*, vol. 24, no. 12, p. 103504, Dec. 2021, doi: 10.1016/j.isci.2021.103504.

[3] B. Liao, W. Zhao, D. R. Beers, J. S. Henkel, and S. H. Appel, 'Transformation from a neuroprotective to a neurotoxic microglial phenotype in a mouse model of ALS', *Exp Neurol*, vol. 237, no. 1, pp. 147–152, Nov. 2012, doi: 10.1016/j.expneurol.2012.06.011.

[4] P. Carninci *et al.*, 'The Transcriptional Landscape of the Mammalian Genome', *Science (1979)*, vol. 309, no. 5740, pp. 1559–1563, Sep. 2005, doi: 10.1126/science.1112014.

[5] L. D. Stein *et al.*, 'The Genome Sequence of Caenorhabditis briggsae: A Platform for Comparative Genomics', *PLoS Biol*, vol. 1, no. 2, p. e45, Nov. 2003, doi: 10.1371/journal.pbio.0000045.

[6] K. v Morris and J. S. Mattick, 'The rise of regulatory RNA.', *Nat Rev Genet*, vol. 15, no. 6, pp. 423–437, Nov. 2014, doi: 10.1038/nrg3722.

[7] A. Fire, S. Xu, M. K. Montgomery, S. A. Kostas, S. E. Driver, and C. C. Mello, 'Potent and specific genetic interference by double-stranded RNA in Caenorhabditis elegans', *Nature*, vol. 391, no. 6669, pp. 806–811, Nov. 1998, doi: 10.1038/35888.

[8] S. M. Hammond, E. Bernstein, D. Beach, and G. J. Hannon, 'An RNA-directed nuclease mediates post-transcriptional gene silencing in Drosophila cells', *Nature*, vol. 404, no. 6775, pp. 293–296, Nov. 2000, doi: 10.1038/35005107.

[9] G. Hutvagner and M. J. Simard, 'Argonaute proteins: key players in RNA silencing', *Nat Rev Mol Cell Biol*, vol. 9, no. 1, pp. 22–32, Nov. 2008, doi: 10.1038/nrm2321.

[10] A. M. Gurtan and P. A. Sharp, 'The Role of miRNAs in Regulating Gene Expression Networks', *J Mol Biol*, vol. 425, no. 19, pp. 3582–3600, Oct. 2013, doi: 10.1016/j.jmb.2013.03.007.

[11] J. J. Quinn and H. Y. Chang, 'Unique features of long non-coding RNA biogenesis and function', *Nat Rev Genet*, vol. 17, no. 1, pp. 47–62, Nov. 2016, doi: 10.1038/nrg.2015.10.

[12] A. A. Bazzini, M. T. Lee, and A. J. Giraldez, 'Ribosome Profiling Shows That miR-430 Reduces Translation Before Causing mRNA Decay in Zebrafish', *Science (1979)*, vol. 336, no. 6078, pp. 233–237, Nov. 2012, doi: 10.1126/science.1215704.

[13] T. A. Volpe, C. Kidner, I. M. Hall, G. Teng, S. I. S. Grewal, and R. A. Martienssen, 'Regulation of Heterochromatic Silencing and Histone H3 Lysine-9 Methylation by RNAi', *Science (1979)*, vol. 297, no. 5588, pp. 1833–1837, Nov. 2002, doi: 10.1126/science.1074973.

[14] M. A. Smith, T. Gesell, P. F. Stadler, and J. S. Mattick, 'Widespread purifying selection on RNA structure in mammals', *Nucleic Acids Res*, vol. 41, no. 17, pp. 8220–8236, Nov. 2013, doi: 10.1093/nar/gkt596.

[15] M. S. Bartolomei, S. Zemel, and S. M. Tilghman, 'Parental imprinting of the mouse H19 gene', *Nature*, vol. 351, no. 6322, pp. 153–155, May 1991, doi: 10.1038/351153a0.

[16] C. J. Brown *et al.*, 'A gene from the region of the human X inactivation centre is expressed exclusively from the inactive X chromosome', *Nature*, vol. 349, no. 6304, pp. 38–44, Jan. 1991, doi: 10.1038/349038a0.

[17] J. M. Engreitz, N. Ollikainen, and M. Guttman, 'Long non-coding RNAs: spatial amplifiers that control nuclear structure and gene expression', *Nat Rev Mol Cell Biol*, vol. 17, no. 12, pp. 756–770, Dec. 2016, doi: 10.1038/nrm.2016.126.

[18] M. Morlando and A. Fatica, 'Alteration of Epigenetic Regulation by Long Noncoding RNAs in Cancer', *Int J Mol Sci*, vol. 19, no. 2, p. 570, Feb. 2018, doi: 10.3390/ijms19020570.

[19] V. Tripathi *et al.*, 'The Nuclear-Retained Noncoding RNA MALAT1 Regulates Alternative Splicing by Modulating SR Splicing Factor Phosphorylation', *Mol Cell*, vol. 39, no. 6, pp. 925–938, Sep. 2010, doi: 10.1016/j.molcel.2010.08.011.

[20] D. Cooper, G. Carter, P. Li, R. Patel, J. Watson, and N. Patel, 'Long Non-Coding RNA NEAT1 Associates with SRp40 to Temporally Regulate PPARγ2 Splicing during Adipogenesis in 3T3-L1 Cells', *Genes (Basel)*, vol. 5, no. 4, pp. 1050–1063, Nov. 2014, doi: 10.3390/genes5041050.

[21] M. Kretz *et al.*, 'Control of somatic tissue differentiation by the long non-coding RNA TINCR', *Nature*, vol. 493, no. 7431, pp. 231–235, Jan. 2013, doi: 10.1038/nature11661.

[22] C. Gong and L. E. Maquat, 'lncRNAs transactivate STAU1-mediated mRNA decay by duplexing with 3′ UTRs via Alu elements', *Nature*, vol. 470, no. 7333, pp. 284–288, Feb. 2011, doi: 10.1038/nature09701.

[23] D. Dimartino *et al.*, 'The Long Non-coding RNA lnc-31 Interacts with Rock1 mRNA and Mediates Its YB-1-Dependent Translation', *Cell Rep*, vol. 23, no. 3, pp. 733–740, Apr. 2018, doi: 10.1016/j.celrep.2018.03.101.

[24] F. Zalfa *et al.*, 'The Fragile X Syndrome Protein FMRP Associates with BC1 RNA and Regulates the Translation of Specific mRNAs at Synapses', *Cell*, vol. 112, no. 3, pp. 317–327, Feb. 2003, doi: 10.1016/S0092-8674(03)00079-5.

[25] J. Zhong *et al.*, 'BC1 Regulation of Metabotropic Glutamate Receptor-Mediated Neuronal Excitability', *Journal of Neuroscience*, vol. 29, no. 32, pp. 9977–9986, Aug. 2009, doi: 10.1523/JNEUROSCI.3893-08.2009.

[26] M. Guttman *et al.*, 'lincRNAs act in the circuitry controlling pluripotency and differentiation', *Nature*, vol. 477, no. 7364, pp. 295–300, Sep. 2011, doi: 10.1038/nature10398.

[27] S.-Y. Ng, R. Johnson, and L. W. Stanton, 'Human long non-coding RNAs promote pluripotency and neuronal differentiation by association with chromatin modifiers and transcription factors', *EMBO J*, vol. 31, no. 3, pp. 522–533, Feb. 2012, doi: 10.1038/emboj.2011.459.

[28] K. W. Vance *et al.*, 'The long non-coding RNA Paupar regulates the expression of both local and distal genes', *EMBO J*, vol. 33, no. 4, pp. 296–311, Feb. 2014, doi: 10.1002/embj.201386225.

[29] B. Salvatori, S. Biscarini, and M. Morlando, 'Non-coding RNAs in Nervous System Development and Disease', *Front Cell Dev Biol*, vol. 8, May 2020, doi: 10.3389/fcell.2020.00273.

[30] Y. Nishimoto *et al.*, 'The long non-coding RNA nuclear-enriched abundant transcript 1_2 induces paraspeckle formation in the motor neuron during the early phase of amyotrophic lateral sclerosis', *Mol Brain*, vol. 6, no. 1, p. 31, 2013, doi: 10.1186/1756-6606-6-31.

[31] H. An, N. G. Williams, and T. A. Shelkovnikova, 'NEAT1 and paraspeckles in neurodegenerative diseases: A missing lnc found?', *Noncoding RNA Res*, vol. 3, no. 4, pp. 243–252, Dec. 2018, doi: 10.1016/j.ncrna.2018.11.003.

[32] M. A. Faghihi *et al.*, 'Evidence for natural antisense transcript-mediated inhibition of microRNA function', *Genome Biol*, vol. 11, no. 5, p. R56, May 2010, doi: 10.1186/gb-2010-11-5-r56.

[33] H. L. Sanger, G. Klotz, D. Riesner, H. J. Gross, and A. K. Kleinschmidt, 'Viroids are single-stranded covalently closed circular RNA molecules existing as highly base-paired rod-like structures.', *Proceedings of the National Academy of Sciences*, vol. 73, no. 11, pp. 3852–3856, Nov. 1976, doi: 10.1073/pnas.73.11.3852.

[34] B. Capel *et al.*, 'Circular transcripts of the testis-determining gene Sry in adult mouse testis', *Cell*, vol. 73, no. 5, pp. 1019–1030, Nov. 1993, doi: 10.1016/0092-8674(93)90279-Y.

[35] E. J. Gardner, Z. F. Nizami, C. C. Talbot, and J. G. Gall, 'Stable intronic sequence RNA (sisRNA), a new class of noncoding RNA from the oocyte nucleus of Xenopus tropicalis.', *Genes Dev*, vol. 26, no. 22, pp. 2550–2559, Nov. 2012, doi: 10.1101/gad.202184.112.

[36] X. You *et al.*, 'Neural circular RNAs are derived from synaptic genes and regulated by development and plasticity', *Nat Neurosci*, vol. 18, no. 4, pp. 603–610, Nov. 2015, doi: 10.1038/nn.3975.

[37] R. Ashwal-Fluss *et al.*, 'circRNA Biogenesis Competes with Pre-mRNA Splicing', *Mol Cell*, vol. 56, no. 1, pp. 55–66, Nov. 2014, doi: 10.1016/J.MOLCEL.2014.08.019.

[38] S. J. Conn *et al.*, 'The RNA Binding Protein Quaking Regulates Formation of circRNAs', *Cell*, vol. 160, no. 6, pp. 1125–1134, Nov. 2015, doi: 10.1016/J.CELL.2015.02.014.

[39] M. C. Kramer *et al.*, 'Combinatorial control of *Drosophila* circular RNA expression by intronic repeats, hnRNPs, and SR proteins', *Genes Dev*, vol. 29, no. 20, pp. 2168–2182, Oct. 2015, doi: 10.1101/gad.270421.115.

[40] L. Errichelli *et al.*, 'FUS affects circular RNA expression in murine embryonic stem cell-derived motor neurons.', *Nat Commun*, vol. 8, no. 1, p. 14741, Nov. 2017, doi: 10.1038/ncomms14741.

[41] T. Fei *et al.*, 'Genome-wide CRISPR screen identifies HNRNPL as a prostate cancer dependency regulating RNA splicing', *Proceedings of the National Academy of Sciences*, vol. 114, no. 26, Jun. 2017, doi: 10.1073/pnas.1617467114.

[42] W. R. Jeck *et al.*, 'Circular RNAs are abundant, conserved, and associated with ALU repeats.', *RNA*, vol. 19, no. 2, pp. 141–157, Nov. 2013, doi: 10.1261/rna.035667.112.

[43] A. Ivanov *et al.*, 'Analysis of Intron Sequences Reveals Hallmarks of Circular RNA Biogenesis in Animals', *Cell Rep*, vol. 10, no. 2, pp. 170–177, Jan. 2015, doi: 10.1016/j.celrep.2014.12.019.

[44] X. Li, L. Yang, and L.-L. Chen, 'The Biogenesis, Functions, and Challenges of Circular RNAs.', *Mol Cell*, vol. 71, no. 3, pp. 428–442, Nov. 2018, doi: 10.1016/j.molcel.2018.06.034.

[45] A. C. Panda *et al.*, 'High-purity circular RNA isolation method (RPAD) reveals vast collection of intronic circRNAs', *Nucleic Acids Res*, vol. 45, no. 12, pp. e116–e116, Nov. 2017, doi: 10.1093/nar/gkx297.

[46] X.-O. Zhang, H.-B. Wang, Y. Zhang, X. Lu, L.-L. Chen, and L. Yang, 'Complementary Sequence-Mediated Exon Circularization', *Cell*, vol. 159, no. 1, pp. 134–147, Sep. 2014, doi: 10.1016/j.cell.2014.09.001.

[47] P. Glažar, P. Papavasileiou, and N. Rajewsky, 'circBase: a database for circular RNAs', *RNA*, vol. 20, no. 11, pp. 1666–1670, Nov. 2014, doi: 10.1261/rna.043687.113.

[48] J. O. Westholm *et al.*, 'Genome-wide Analysis of Drosophila Circular RNAs Reveals Their Structural and Sequence Properties and Age-Dependent Neural Accumulation', *Cell Rep*, vol. 9, no. 5, pp. 1966–1980, Dec. 2014, doi: 10.1016/j.celrep.2014.10.062.

[49] T. B. Hansen, 'Improved circRNA Identification by Combining Prediction Algorithms', *Front Cell Dev Biol*, vol. 6, Mar. 2018, doi: 10.3389/fcell.2018.00020.

[50] X.-O. Zhang *et al.*, 'Diverse alternative back-splicing and alternative splicing landscape of circular RNAs.', *Genome Res*, vol. 26, no. 9, pp. 1277–1287, Nov. 2016, doi: 10.1101/gr.202895.115.

[51] L.-T. Gou, P. Dai, and M.-F. Liu, 'Small noncoding RNAs and male infertility', *Wiley Interdiscip Rev RNA*, vol. 5, no. 6, pp. 733–745, Nov. 2014, doi: 10.1002/wrna.1252.

[52] A. Rybak-Wolf *et al.*, 'Circular RNAs in the Mammalian Brain Are Highly Abundant, Conserved, and Dynamically Expressed', *Mol Cell*, vol. 58, no. 5, pp. 870–885, Nov. 2015, doi: 10.1016/j.molcel.2015.03.027.

[53] M. T. Venø *et al.*, 'Spatio-temporal regulation of circular RNA expression during porcine embryonic brain development', *Genome Biol*, vol. 16, no. 1, p. 245, Dec. 2015, doi: 10.1186/s13059-015-0801-3.

[54] D. Liang *et al.*, 'The Output of Protein-Coding Genes Shifts to Circular RNAs When the Pre-mRNA Processing Machinery Is Limiting', *Mol Cell*, vol. 68, no. 5, pp. 940-954.e3, Nov. 2017, doi: 10.1016/J.MOLCEL.2017.10.034.

[55] Y. Enuka, M. Lauriola, M. E. Feldman, A. Sas-Chen, I. Ulitsky, and Y. Yarden, 'Circular RNAs are long-lived and display only minimal early alterations in response to a growth factor', *Nucleic Acids Res*, vol. 44, no. 3, pp. 1370–1383, Nov. 2016, doi: 10.1093/nar/gkv1367.

[56] T. B. Hansen *et al.*, 'miRNA-dependent gene silencing involving Ago2-mediated cleavage of a circular antisense RNA', *EMBO J*, vol. 30, no. 21, pp. 4414–4422, Nov. 2011, doi: 10.1038/emboj.2011.359.

[57] T. B. Hansen *et al.*, 'Natural RNA circles function as efficient microRNA sponges', *Nature*, vol. 495, no. 7441, pp. 384–388, Mar. 2013, doi: 10.1038/nature11993.

[58] S. Kelly, C. Greenman, P. R. Cook, and A. Papantonis, 'Exon Skipping Is Correlated with Exon Circularization', *J Mol Biol*, vol. 427, no. 15, pp. 2414–2417, Nov. 2015, doi: 10.1016/J.JMB.2015.02.018.

[59] Z. Li *et al.*, 'Exon-intron circular RNAs regulate transcription in the nucleus', *Nat Struct Mol Biol*, vol. 22, no. 3, pp. 256–264, Nov. 2015, doi: 10.1038/nsmb.2959.

[60] Z.-Y. Zou *et al.*, 'De novo FUS gene mutations are associated with juvenile-onset sporadic amyotrophic lateral sclerosis in China', *Neurobiol Aging*, vol. 34, no. 4, pp. 1312.e1-1312.e8, Nov. 2013, doi: 10.1016/J.NEUROBIOLAGING.2012.09.005.

[61] V. M. Conn, V. Hugouvieux, A. Nayak, S. A. C.-N. plants, and undefined 2017, 'A circRNA from SEPALLATA3 regulates splicing of its cognate mRNA through R-loop formation', *nature.com*, [Online]. Available: https://www.nature.com/articles/nplants201753

[62] I. Legnini *et al.*, 'Circ-ZNF609 Is a Circular RNA that Can Be Translated and Functions in Myogenesis', *Mol Cell*, vol. 66, no. 1, pp. 22-37.e9, Nov. 2017, doi: 10.1016/J.MOLCEL.2017.02.017.

[63] Y. Yang *et al.*, 'Extensive translation of circular RNAs driven by N6-methyladenosine', *Cell Res*, vol. 27, no. 5, pp. 626–641, Nov. 2017, doi: 10.1038/cr.2017.31.

[64] E. D'Ambra, D. Capauto, and M. Morlando, 'Exploring the Regulatory Role of Circular RNAs in Neurodegenerative Disorders', *Int J Mol Sci*, vol. 20, no. 21, p. 5477, Nov. 2019, doi: 10.3390/ijms20215477.

[65] W. J. Lukiw, 'Circular RNA (circRNA) in Alzheimer's disease (AD)', *Front Genet*, vol. 4, p. 307, 2013, doi: 10.3389/fgene.2013.00307.

[66] Y. G. Chen *et al.*, 'Sensing Self and Foreign Circular RNAs by Intron Identity', *Mol Cell*, vol. 67, no. 2, pp. 228-238.e5, Nov. 2017, doi: 10.1016/J.MOLCEL.2017.05.022.

[67] O. Hardiman *et al.*, 'Amyotrophic lateral sclerosis', *Nat Rev Dis Primers*, vol. 3, p. 17071, Nov. 2017, doi: 10.1038/nrdp.2017.71.

[68] J. M. Winhammar, D. B. Rowe, R. D. Henderson, and M. C. Kiernan, 'Assessment of disease progression in motor neuron disease', *Lancet Neurol*, vol. 4, no. 4, pp. 229–238, Apr. 2005, doi: 10.1016/S1474-4422(05)70042-9.

[69] M. J. Greenway *et al.*, 'ANG mutations segregate with familial and "sporadic" amyotrophic lateral sclerosis', *Nat Genet*, vol. 38, no. 4, pp. 411–413, Nov. 2006, doi: 10.1038/ng1742.

[70] K. Abhinav *et al.*, 'Amyotrophic Lateral Sclerosis in South-East England: A Population-Based Study', *Neuroepidemiology*, vol. 29, no. 1–2, pp. 44–48, 2007, doi: 10.1159/000108917.

[71] C. G. Goetz, 'Amyotrophic lateral sclerosis: early contributions of Jean-Martin Charcot.', *Muscle Nerve*, vol. 23, no. 3, pp. 336–343, Nov. 2000, doi: 10.1002/(sici)1097-4598(200003)23:3<336::aid-mus4>3.0.co;2-l.

[72] L. C. Wijesekera and P. N. Leigh, 'Amyotrophic lateral sclerosis', *Orphanet J Rare Dis*, vol. 4, no. 1, p. 3, Nov. 2009, doi: 10.1186/1750-1172-4-3.

[73] G. Logroscino *et al.*, 'Descriptive epidemiology of amyotrophic lateral sclerosis: new evidence and unsolved issues', *J Neurol Neurosurg Psychiatry*, vol. 79, no. 1, pp. 6–11, Nov. 2008, doi: 10.1136/jnnp.2006.104828.

[74] P. Shaw and C. J. Eggett, 'Molecular factors underlying selective vulnerability of motor neurons to neurodegeneration in amyotrophic lateral sclerosis', *J Neurol*, vol. 247, no. S1, pp. I17–I27, Nov. 2000, doi: 10.1007/BF03161151.

[75] M. Neumann *et al.*, 'Ubiquitinated TDP-43 in Frontotemporal Lobar Degeneration and Amyotrophic Lateral Sclerosis', *Science (1979)*, vol. 314, no. 5796, pp. 130–133, Nov. 2006, doi: 10.1126/science.1134108.

[76] J. Phukan *et al.*, 'The syndrome of cognitive impairment in amyotrophic lateral sclerosis: a population-based study', *J Neurol Neurosurg Psychiatry*, vol. 83, no. 1, pp. 102–108, Nov. 2012, doi: 10.1136/jnnp-2011-300188.

[77] M. G. Weisskopf *et al.*, 'Prospective study of chemical exposures and amyotrophic lateral sclerosis', *J Neurol Neurosurg Psychiatry*, vol. 80, no. 5, pp. 558–561, Nov. 2009, doi: 10.1136/jnnp.2008.156976.

[78] Y.-Z. Chen *et al.*, 'DNA/RNA Helicase Gene Mutations in a Form of Juvenile Amyotrophic Lateral Sclerosis (ALS4)', *The American Journal of Human Genetics*, vol. 74, no. 6, pp. 1128–1135, Nov. 2004, doi: 10.1086/421054.

[79] E. Beghi *et al.*, 'The epidemiology and treatment of ALS: Focus on the heterogeneity of the disease and critical appraisal of therapeutic trials', *Amyotrophic Lateral Sclerosis*, vol. 12, no. 1, pp. 1–10, Jan. 2011, doi: 10.3109/17482968.2010.502940.

[80] W. van Rheenen *et al.*, 'Genome-wide association analyses identify new risk variants and the genetic architecture of amyotrophic lateral sclerosis', *Nat Genet*, vol. 48, no. 9, pp. 1043–1048, Nov. 2016, doi: 10.1038/ng.3622.

[81] K. Forsberg, P. M. Andersen, S. L. Marklund, and T. Brännström, 'Glial nuclear aggregates of superoxide dismutase-1 are regularly present in patients with amyotrophic lateral sclerosis', *Acta Neuropathol*, vol. 121, no. 5, pp. 623–634, Nov. 2011, doi: 10.1007/s00401-011-0805-3.

[82] K. J. de Vos *et al.*, 'Familial amyotrophic lateral sclerosis-linked SOD1 mutants perturb fast axonal transport to reduce axonal mitochondria content', *Hum Mol Genet*, vol. 16, no. 22, pp. 2720–2728, Nov. 2007, doi: 10.1093/hmg/ddm226.

[83] M. J. Chung and Y.-L. Suh, 'Ultrastructural Changes of Mitochondria in the Skeletal Muscle of Patients with Amyotrophic Lateral Sclerosis', *Ultrastruct Pathol*, vol. 26, no. 1, pp. 3–7, Nov. 2002, doi: 10.1080/01913120252934260.

[84] S. Boillée, C. vande Velde, and D. W. Cleveland, 'ALS: A Disease of Motor Neurons and Their Nonneuronal Neighbors', *Neuron*, vol. 52, no. 1, pp. 39–59, Nov. 2006, doi: 10.1016/j.neuron.2006.09.018.

[85] J. Magrané and G. Manfredi, 'Mitochondrial function, morphology, and axonal transport in amyotrophic lateral sclerosis.', *Antioxid Redox Signal*, vol. 11, no. 7, pp. 1615–1626, Nov. 2009, doi: 10.1089/ARS.2009.2604.

[86] K. Ikenaka, M. Katsuno, K. Kawai, S. Ishigaki, F. Tanaka, and G. Sobue, 'Disruption of axonal transport in motor neuron diseases.', *Int J Mol Sci*, vol. 13, no. 1, pp. 1225–1238, 2012, doi: 10.3390/ijms13011225.

[87] C. P. Webster *et al.*, 'The C9orf72 protein interacts with Rab1a and the ULK 1 complex to regulate initiation of autophagy', *EMBO J*, vol. 35, no. 15, pp. 1656–1676, Nov. 2016, doi: 10.15252/embj.201694401.

[88] M. J. Walsh, G. M. Hautbergue, and S. A. Wilson, 'Structure and function of mRNA export adaptors', *Biochem Soc Trans*, vol. 38, no. 1, pp. 232–236, Nov. 2010, doi: 10.1042/BST0380232.

[89] J. Cooper-Knock *et al.*, 'Sequestration of multiple RNA recognition motif-containing proteins by C9orf72 repeat expansions', *Brain*, vol. 137, no. 7, pp. 2040–2051, Nov. 2014, doi: 10.1093/brain/awu120.

[90] B. M. Schwenk *et al.*, 'TDP-43 loss of function inhibits endosomal trafficking and alters trophic signaling in neurons', *EMBO J*, vol. 35, no. 21, pp. 2350–2370, Nov. 2016, doi: 10.15252/embj.201694221.

[91] L. Pasquali, P. Lenzi, F. Biagioni, G. Siciliano, and F. Fornai, 'Cell to Cell Spreading of Misfolded Proteins as a Therapeutic Target in Motor Neuron Disease', *Curr Med Chem*, vol. 21, no. 31, pp. 3508–3534, Nov. 2014, doi: 10.2174/0929867321666140601161534.

[92] A. E. Conicella, G. H. Zerze, J. Mittal, and N. L. Fawzi, 'ALS Mutations Disrupt Phase Separation Mediated by α-Helical Structure in the TDP-43 Low-Complexity C-Terminal Domain', *Structure*, vol. 24, no. 9, pp. 1537–1549, Nov. 2016, doi: 10.1016/j.str.2016.07.007.

[93] E. S. Arnold *et al.*, 'ALS-linked TDP-43 mutations produce aberrant RNA splicing and adult-onset motor neuron disease without aggregation or loss of nuclear TDP-43', *Proceedings of the National Academy of Sciences*, vol. 110, no. 8, pp. E736–E745, Nov. 2013, doi: 10.1073/pnas.1222809110.

[94] A. S. Chen-Plotkin, V. M.-Y. Lee, and J. Q. Trojanowski, 'TAR DNA-binding protein 43 in neurodegenerative disease.', *Nat Rev Neurol*, vol. 6, no. 4, pp. 211–220, Nov. 2010, doi: 10.1038/nrneurol.2010.18.

[95] Y. Zhou, S. Liu, A. Öztürk, and G. G. Hicks, 'FUS-regulated RNA metabolism and DNA damage repair', *Rare Diseases*, vol. 2, no. 1, p. e29515, Nov. 2014, doi: 10.4161/rdis.29515.

[96] A. Amlie-Wolf *et al.*, 'Transcriptomic Changes Due to Cytoplasmic TDP-43 Expression Reveal Dysregulation of Histone Transcripts and Nuclear Chromatin', *PLoS One*, vol. 10, no. 10, p. e0141836, Nov. 2015, doi: 10.1371/journal.pone.0141836.

[97] S. J. Parker *et al.*, 'Endogenous TDP-43 localized to stress granules can subsequently form protein aggregates', *Neurochem Int*, vol. 60, no. 4, pp. 415–424, Nov. 2012, doi: 10.1016/j.neuint.2012.01.019.

[98] A. Aguzzi and L. Rajendran, 'The Transcellular Spread of Cytosolic Amyloids, Prions, and Prionoids', *Neuron*, vol. 64, no. 6, pp. 783–790, Nov. 2009, doi: 10.1016/j.neuron.2009.12.016.

[99] M. Polymenidou and D. W. Cleveland, 'The seeds of neurodegeneration: prion-like spreading in ALS.', *Cell*, vol. 147, no. 3, pp. 498–508, Nov. 2011, doi: 10.1016/j.cell.2011.10.011.

[100] C. Lagier-Tourenne, M. Polymenidou, and D. W. Cleveland, 'TDP-43 and FUS/TLS: emerging roles in RNA processing and neurodegeneration', *Hum Mol Genet*, vol. 19, no. R1, pp. R46–R64, Nov. 2010, doi: 10.1093/hmg/ddq137.

[101] H. Zinszner, J. Sok, D. Immanuel, Y. Yin, and D. Ron, 'TLS (FUS) binds RNA in vivo and engages in nucleo-cytoplasmic shuttling.', *J Cell Sci*, vol. 110 (Pt 15), no. 15, pp. 1741–1750, Nov. 1997, doi: 10.1242/jcs.00927.

[102] A. Bertolotti, Y. Lutz, D. J. Heard, P. Chambon, and L. Tora, 'hTAF(II)68, a novel RNA/ssDNA-binding protein with homology to the pro-oncoproteins TLS/FUS and EWS is associated with both TFIID and RNA polymerase II.', *EMBO J*, vol. 15, no. 18, pp. 5022–5031, Nov. 1996, [Online]. Available: http://www.ncbi.nlm.nih.gov/pubmed/8890175

[103] I. Kwon *et al.*, 'Phosphorylation-Regulated Binding of RNA Polymerase II to Fibrous Polymers of Low-Complexity Domains', *Cell*, vol. 155, no. 5, pp. 1049–1060, Nov. 2013, doi: 10.1016/j.cell.2013.10.033.

[104] A. S. Mastrocola, S. H. Kim, A. T. Trinh, L. A. Rodenkirch, and R. S. Tibbetts, 'The RNA-binding Protein Fused in Sarcoma (FUS) Functions Downstream of Poly(ADP-ribose) Polymerase (PARP) in Response to DNA Damage', *Journal of Biological Chemistry*, vol. 288, no. 34, pp. 24731–24741, Nov. 2013, doi: 10.1074/jbc.M113.497974.

[105] S. L. Rulten *et al.*, 'PARP-1 dependent recruitment of the amyotrophic lateral sclerosis-associated protein FUS/TLS to sites of oxidative DNA damage', *Nucleic Acids Res*, vol. 42, no. 1, pp. 307–314, Nov. 2014, doi: 10.1093/nar/gkt835.

[106] D. D. Prasad, M. Ouchida, L. Lee, V. N. Rao, and E. S. Reddy, 'TLS/FUS fusion domain of TLS/FUS-erg chimeric protein resulting from the t(16;21) chromosomal translocation in human myeloid leukemia functions as a transcriptional activation domain.', *Oncogene*, vol. 9, no. 12, pp. 3717–3729, Nov. 1994, [Online]. Available: http://www.ncbi.nlm.nih.gov/pubmed/7970732

[107] D. Orozco and D. Edbauer, 'FUS-mediated alternative splicing in the nervous system: consequences for ALS and FTLD', *J Mol Med*, vol. 91, no. 12, pp. 1343–1354, Nov. 2013, doi: 10.1007/s00109-013-1077-2.

[108] S. Wu and M. R. Green, 'Identification of a human protein that recognizes the 3' splice site during the second step of pre-mRNA splicing.', *EMBO J*, vol. 16, no. 14, pp. 4421–4432, Nov. 1997, doi: 10.1093/emboj/16.14.4421.

[109] Y. Zhou, S. Liu, G. Liu, A. Öztürk, and G. G. Hicks, 'ALS-Associated FUS Mutations Result in Compromised FUS Alternative Splicing and Autoregulation', *PLoS Genet*, vol. 9, no. 10, p. e1003895, Nov. 2013, doi: 10.1371/journal.pgen.1003895.

[110] S. Dini Modigliani, M. Morlando, L. Errichelli, M. Sabatelli, and I. Bozzoni, 'An ALS-associated mutation in the FUS 3′-UTR disrupts a microRNA–FUS regulatory circuitry', *Nat Commun*, vol. 5, no. 1, p. 4335, Sep. 2014, doi: 10.1038/ncomms5335.

[111] R. I. Gregory *et al.*, 'The Microprocessor complex mediates the genesis of microRNAs', *Nature*, vol. 432, no. 7014, pp. 235–240, Nov. 2004, doi: 10.1038/nature03120.

[112] M. Morlando *et al.*, 'FUS stimulates microRNA biogenesis by facilitating co-transcriptional Drosha recruitment', *EMBO J*, vol. 31, no. 24, pp. 4502–4510, Nov. 2012, doi: 10.1038/emboj.2012.319.

[113] Y. M. Ayala, T. Misteli, and F. E. Baralle, 'TDP-43 regulates retinoblastoma protein phosphorylation through the repression of cyclin-dependent kinase 6 expression', *Proceedings of the National Academy of Sciences*, vol. 105, no. 10, pp. 3785–3789, Nov. 2008, doi: 10.1073/pnas.0800546105.

[114] P. Anderson and N. Kedersha, 'RNA granules: post-transcriptional and epigenetic modulators of gene expression', *Nat Rev Mol Cell Biol*, vol. 10, no. 6, pp. 430–436, Nov. 2009, doi: 10.1038/nrm2694.

[115] R. Fujii and T. Takumi, 'TLS facilitates transport of mRNA encoding an actin-stabilizing protein to dendritic spines', *J Cell Sci*, vol. 118, no. 24, pp. 5755–5765, Dec. 2005, doi: 10.1242/jcs.02692.

[116] R. Fujii *et al.*, 'The RNA Binding Protein TLS Is Translocated to Dendritic Spines by mGluR5 Activation and Regulates Spine Morphology', *Current Biology*, vol. 15, no. 6, pp. 587–593, Nov. 2005, doi: 10.1016/j.cub.2005.01.058.

[117] A. Belly, F. Moreau-Gachelin, R. Sadoul, and Y. Goldberg, 'Delocalization of the multifunctional RNA splicing factor TLS/FUS in hippocampal neurones: exclusion from the nucleus and accumulation in dendritic granules and spine heads', *Neurosci Lett*, vol. 379, no. 3, pp. 152–157, Nov. 2005, doi: 10.1016/j.neulet.2004.12.071.

[118] K. Yasuda, S. F. Clatterbuck-Soper, M. E. Jackrel, J. Shorter, and S. Mili, 'FUS inclusions disrupt RNA localization by sequestering kinesin-1 and inhibiting microtubule detyrosination', *Journal of Cell Biology*, vol. 216, no. 4, pp. 1015–1034, Apr. 2017, doi: 10.1083/jcb.201608022.

[119] D. Deshpande *et al.*, 'Synaptic FUS Localization During Motoneuron Development and Its Accumulation in Human ALS Synapses', *Front Cell Neurosci*, vol. 13, Jun. 2019, doi: 10.3389/fncel.2019.00256.

[120] H.-R. Li, W.-C. Chiang, P.-C. Chou, W.-J. Wang, and J. Huang, 'TAR DNA-binding protein 43 (TDP-43) liquid–liquid phase separation is mediated by just a few aromatic residues', *Journal of Biological Chemistry*, vol. 293, no. 16, pp. 6090–6098, Apr. 2018, doi: 10.1074/jbc.AC117.001037.

[121] A. Molliex *et al.*, 'Phase Separation by Low Complexity Domains Promotes Stress Granule Assembly and Drives Pathological Fibrillization', *Cell*, vol. 163, no. 1, pp. 123–133, Nov. 2015, doi: 10.1016/j.cell.2015.09.015.

[122] A. Patel *et al.*, 'A Liquid-to-Solid Phase Transition of the ALS Protein FUS Accelerated by Disease Mutation', *Cell*, vol. 162, no. 5, pp. 1066–1077, Aug. 2015, doi: 10.1016/j.cell.2015.07.047.

[123] J. L. Carey and L. Guo, 'Liquid-Liquid Phase Separation of TDP-43 and FUS in Physiology and Pathology of Neurodegenerative Diseases', *Front Mol Biosci*, vol. 9, Feb. 2022, doi: 10.3389/fmolb.2022.826719.

[124] Z. R. Grese, A. C. Bastos, L. D. Mamede, R. L. French, T. M. Miller, and Y. M. Ayala, 'Specific RNA interactions promote TDP-43 multivalent phase separation and maintain liquid properties', *EMBO Rep*, vol. 22, no. 12, Dec. 2021, doi: 10.15252/embr.202153632.

[125] K. A. Burke, A. M. Janke, C. L. Rhine, and N. L. Fawzi, 'Residue-by-Residue View of In Vitro FUS Granules that Bind the C-Terminal Domain of RNA Polymerase II', *Mol Cell*, vol. 60, no. 2, pp. 231–241, Oct. 2015, doi: 10.1016/j.molcel.2015.09.006.

[126] J. C. Schwartz, X. Wang, E. R. Podell, and T. R. Cech, 'RNA Seeds Higher-Order Assembly of FUS Protein', *Cell Rep*, vol. 5, no. 4, pp. 918–925, Nov. 2013, doi: 10.1016/j.celrep.2013.11.017.

[127] Z. M. March, O. D. King, and J. Shorter, 'Prion-like domains as epigenetic regulators, scaffolds for subcellular organization, and drivers of neurodegenerative disease', *Brain Res*, vol. 1647, pp. 9–18, Sep. 2016, doi: 10.1016/j.brainres.2016.02.037.

[128] M. Kato *et al.*, 'Cell-free Formation of RNA Granules: Low Complexity Sequence Domains Form Dynamic Fibers within Hydrogels', *Cell*, vol. 149, no. 4, pp. 753–767, Nov. 2012, doi: 10.1016/j.cell.2012.04.017.

[129] M. Kato and S. L. McKnight, 'The low-complexity domain of the FUS RNA binding protein self-assembles via the mutually exclusive use of two distinct cross-β cores', *Proceedings of the National Academy of Sciences*, vol. 118, no. 42, Oct. 2021, doi: 10.1073/pnas.2114412118.

[130] Y. Lin, D. S. W. Protter, M. K. Rosen, and R. Parker, 'Formation and Maturation of Phase-Separated Liquid Droplets by RNA-Binding Proteins', *Mol Cell*, vol. 60, no. 2, pp. 208–219, Nov. 2015, doi: 10.1016/j.molcel.2015.08.018.

[131] M. I. Martinez-Macias *et al.*, 'FUS (fused in sarcoma) is a component of the cellular response to topoisomerase I–induced DNA breakage and transcriptional stress', *Life Sci Alliance*, vol. 2, no. 2, p. e201800222, Apr. 2019, doi: 10.26508/lsa.201800222.

[132] S. Hennig *et al.*, 'Prion-like domains in RNA binding proteins are essential for building subnuclear paraspeckles', *Journal of Cell Biology*, vol. 210, no. 4, pp. 529–539, Aug. 2015, doi: 10.1083/jcb.201504117.

[133] J. A. West *et al.*, 'Structural, super-resolution microscopy analysis of paraspeckle nuclear body organization', *Journal of Cell Biology*, vol. 214, no. 7, pp. 817–830, Sep. 2016, doi: 10.1083/jcb.201601071.

[134] T. A. Shelkovnikova, H. K. Robinson, C. Troakes, N. Ninkina, and V. L. Buchman, 'Compromised paraspeckle formation as a pathogenic factor in FUSopathies', *Hum Mol Genet*, vol. 23, no. 9, pp. 2298–2312, May 2014, doi: 10.1093/hmg/ddt622.

[135] S. Jain, J. R. Wheeler, R. W. Walters, A. Agrawal, A. Barsic, and R. Parker, 'ATPase-Modulated Stress Granules Contain a Diverse Proteome and Substructure', *Cell*, vol. 164, no. 3, pp. 487–498, Nov. 2016, doi: 10.1016/j.cell.2015.12.038.

[136] N. Kedersha *et al.*, 'Stress granules and processing bodies are dynamically linked sites of mRNP remodeling', *J Cell Biol*, vol. 169, no. 6, pp. 871–884, Nov. 2005, doi: 10.1083/jcb.200502088.

[137] J. R. Buchan and R. Parker, 'Eukaryotic Stress Granules: The Ins and Outs of Translation', *Mol Cell*, vol. 36, no. 6, pp. 932–941, Dec. 2009, doi: 10.1016/j.molcel.2009.11.020.

[138] P. Anderson and N. Kedersha, 'Stress granules: the Tao of RNA triage', *Trends Biochem Sci*, vol. 33, no. 3, pp. 141–150, Nov. 2008, doi: 10.1016/J.TIBS.2007.12.003.

[139] E. Boye and B. Grallert, 'eIF2α phosphorylation and the regulation of translation', *Curr Genet*, vol. 66, no. 2, pp. 293–297, Apr. 2020, doi: 10.1007/s00294-019-01026-1.

[140] H. P. Harding *et al.*, 'An Integrated Stress Response Regulates Amino Acid Metabolism and Resistance to Oxidative Stress', *Mol Cell*, vol. 11, no. 3, pp. 619–633, Mar. 2003, doi: 10.1016/S1097-2765(03)00105-9.

[141] K. Pakos-Zebrucka, I. Koryga, K. Mnich, M. Ljujic, A. Samali, and A. M. Gorman, 'The integrated stress response', *EMBO Rep*, vol. 17, no. 10, pp. 1374–1395, Oct. 2016, doi: 10.15252/embr.201642195.

[142] N. Gilks *et al.*, 'Stress Granule Assembly Is Mediated by Prion-like Aggregation of TIA-1', *Mol Biol Cell*, vol. 15, no. 12, pp. 5383–5398, Nov. 2004, doi: 10.1091/mbc.e04-08-0715.

[143] T. Ohn, N. Kedersha, T. Hickman, S. Tisdale, and P. Anderson, 'A functional RNAi screen links O-GlcNAc modification of ribosomal proteins to stress granule and processing body assembly.', *Nat Cell Biol*, vol. 10, no. 10, pp. 1224–1231, Nov. 2008, doi: 10.1038/ncb1783.

[144] S. Solomon *et al.*, 'Distinct Structural Features ofCaprin-1 Mediate Its Interaction with G3BP-1 and Its Induction of Phosphorylation of Eukaryotic Translation Initiation Factor 2α, Entry to Cytoplasmic Stress Granules, and Selective Interaction with a Subset of mRNAs', *Mol Cell Biol*, vol. 27, no. 6, pp. 2324–2342, Nov. 2007, doi: 10.1128/MCB.02300-06.

[145] N. Kedersha *et al.*, 'G3BP–Caprin1–USP10 complexes mediate stress granule condensation and associate with 40S subunits', *J Cell Biol*, vol. 212, no. 7, pp. 845–860, Nov. 2016, doi: 10.1083/jcb.201508028.

[146] J. R. Buchan, D. Muhlrad, and R. Parker, 'P bodies promote stress granule assembly in *Saccharomyces cerevisiae*', *J Cell Biol*, vol. 183, no. 3, pp. 441–455, Nov. 2008, doi: 10.1083/jcb.200807043.

[147] H. Tourrière *et al.*, 'The RasGAP-associated endoribonuclease G3BP assembles stress granules', *J Cell Biol*, vol. 160, no. 6, pp. 823–831, Nov. 2003, doi: 10.1083/jcb.200212128.

[148] S. L. Moon, T. Morisaki, A. Khong, K. Lyon, R. Parker, and T. J. Stasevich, 'Multicolour single-molecule tracking of mRNA interactions with RNP granules', *Nat Cell Biol*, vol. 21, no. 2, pp. 162–168, Feb. 2019, doi: 10.1038/s41556-018-0263-4.

[149] D. Mateju, B. Eichenberger, F. Voigt, J. Eglinger, G. Roth, and J. A. Chao, 'Single-Molecule Imaging Reveals Translation of mRNAs Localized to Stress Granules', *Cell*, vol. 183, no. 7, pp. 1801-1812.e13, Dec. 2020, doi: 10.1016/j.cell.2020.11.010.

[150] P. Ivanov, N. Kedersha, and P. Anderson, 'Stress Granules and Processing Bodies in Translational Control', *Cold Spring Harb Perspect Biol*, vol. 11, no. 5, p. a032813, May 2019, doi: 10.1101/cshperspect.a032813.

[151] M. D. Panas, P. Ivanov, and P. Anderson, 'Mechanistic insights into mammalian stress granule dynamics', *Journal of Cell Biology*, vol. 215, no. 3, pp. 313–323, Nov. 2016, doi: 10.1083/jcb.201609081.

[152] B. Wolozin and P. Ivanov, 'Stress granules and neurodegeneration', *Nat Rev Neurosci*, vol. 20, no. 11, pp. 649–666, Nov. 2019, doi: 10.1038/s41583-019-0222-5.

[153] A. Aizer, Y. Brody, L. W. Ler, N. Sonenberg, R. H. Singer, and Y. Shav-Tal, 'The Dynamics of Mammalian P Body Transport, Assembly, and Disassembly In Vivo', *Mol Biol Cell*, vol. 19, no. 10, pp. 4154–4166, Nov. 2008, doi: 10.1091/mbc.e08-05-0513.

[154] A. K. L. Leung, J. M. Calabrese, and P. A. Sharp, 'Quantitative analysis of Argonaute protein reveals microRNA-dependent localization to stress granules', *Proceedings of the National Academy of Sciences*, vol. 103, no. 48, pp. 18125–18130, Nov. 2006, doi: 10.1073/pnas.0608845103.

[155] M. Ramaswami, J. P. Taylor, and R. Parker, 'Altered Ribostasis: RNA-Protein Granules in Degenerative Disorders', *Cell*, vol. 154, no. 4, pp. 727–736, Nov. 2013, doi: 10.1016/j.cell.2013.07.038.

[156] R. W. Walters, D. Muhlrad, J. Garcia, and R. Parker, 'Differential effects of Ydj1 and Sis1 on Hsp70-mediated clearance of stress granules in *Saccharomyces cerevisiae*', *RNA*, vol. 21, no. 9, pp. 1660–1671, Nov. 2015, doi: 10.1261/rna.053116.115.

[157] T. J. Kwiatkowski *et al.*, 'Mutations in the FUS/TLS Gene on Chromosome 16 Cause Familial Amyotrophic Lateral Sclerosis', *Science (1979)*, vol. 323, no. 5918, pp. 1205–1208, Nov. 2009, doi: 10.1126/science.1166066.

[158] E. Bertrand, P. Chartrand, M. Schaefer, S. M. Shenoy, R. H. Singer, and R. M. Long, 'Localization of ASH1 mRNA Particles in Living Yeast', *Mol Cell*, vol. 2, no. 4, pp. 437–445, Oct. 1998, doi: 10.1016/S1097-2765(00)80143-4.

[159] X. Darzacq *et al.*, 'In vivo dynamics of RNA polymerase II transcription', *Nat Struct Mol Biol*, vol. 14, no. 9, pp. 796–806, Sep. 2007, doi: 10.1038/nsmb1280.

[160] E. Tutucci, N. M. Livingston, R. H. Singer, and B. Wu, 'Imaging mRNA In Vivo, from Birth to Death', *Annu Rev Biophys*, vol. 47, no. 1, pp. 85–106, May 2018, doi: 10.1146/annurev-biophys-070317-033037.

[161] P. Le, N. Ahmed, and G. W. Yeo, 'Illuminating RNA biology through imaging', *Nat Cell Biol*, vol. 24, no. 6, pp. 815–824, Jun. 2022, doi: 10.1038/s41556-022-00933-9.

[162] C. Cui, W. Shu, and P. Li, 'Fluorescence In situ Hybridization: Cell-Based Genetic Diagnostic and Research Applications', *Front Cell Dev Biol*, vol. 4, Sep. 2016, doi: 10.3389/fcell.2016.00089.

[163] R. H. Singer and D. C. Ward, 'Actin gene expression visualized in chicken muscle tissue culture by using in situ hybridization with a biotinated nucleotide analog.', *Proceedings of the National Academy of Sciences*, vol. 79, no. 23, pp. 7331–7335, Dec. 1982, doi: 10.1073/pnas.79.23.7331.

[164] A. Raj, P. van den Bogaard, S. A. Rifkin, A. van Oudenaarden, and S. Tyagi, 'Imaging individual mRNA molecules using multiple singly labeled probes', *Nat Methods*, vol. 5, no. 10, pp. 877–879, Oct. 2008, doi: 10.1038/nmeth.1253.

[165] C. Larsson, I. Grundberg, O. Söderberg, and M. Nilsson, 'In situ detection and genotyping of individual mRNA molecules', *Nat Methods*, vol. 7, no. 5, pp. 395–397, Nov. 2010, doi: 10.1038/nmeth.1448.

[166] C. Larsson *et al.*, 'In situ genotyping individual DNA molecules by target-primed rolling-circle amplification of padlock probes', *Nat Methods*, vol. 1, no. 3, pp. 227–232, Dec. 2004, doi: 10.1038/nmeth723.

[167] E. Lubeck, A. F. Coskun, T. Zhiyentayev, M. Ahmad, and L. Cai, 'Single-cell in situ RNA profiling by sequential hybridization.', *Nat Methods*, vol. 11, no. 4, pp. 360–361, Nov. 2014, doi: 10.1038/nmeth.2892.

[168] S. H. Rouhanifard *et al.*, 'ClampFISH detects individual nucleic acid molecules using click chemistry–based amplification', *Nat Biotechnol*, vol. 37, no. 1, pp. 84–89, Jan. 2019, doi: 10.1038/nbt.4286.

[169] F. Wang *et al.*, 'RNAscope', *The Journal of Molecular Diagnostics*, vol. 14, no. 1, pp. 22–29, Jan. 2012, doi: 10.1016/j.jmoldx.2011.08.002.

[170] B. M. Lunde, C. Moore, and G. Varani, 'RNA-binding proteins: modular design for efficient function', *Nat Rev Mol Cell Biol*, vol. 8, no. 6, pp. 479–490, Nov. 2007, doi: 10.1038/nrm2178.

[171] T. Santini, J. Martone, and M. Ballarino, 'Visualization of Nuclear and Cytoplasmic Long Noncoding RNAs at Single-Cell Level by RNA-FISH', 2021, pp. 251–280. doi: 10.1007/978-1-0716-0664-3_15.

[172] V. Vautrot, C. Aigueperse, C. Branlant, and I. Behm-Ansmant, 'Fluorescence In Situ Hybridization of Small Non-Coding RNAs', 2015, pp. 73–83. doi: 10.1007/978-1-4939-2547-6_8.

[173] M. Hinten, E. Maclary, S. Gayen, C. Harris, and S. Kalantry, 'Visualizing Long Noncoding RNAs on Chromatin', 2016, pp. 147–164. doi: 10.1007/978-1-4939-3378-5_12.

[174] P. R. Bejugam, A. Das, and A. C. Panda, 'Seeing Is Believing: Visualizing Circular RNAs', *Noncoding RNA*, vol. 6, no. 4, p. 45, Nov. 2020, doi: 10.3390/ncrna6040045.

[175] A. F. Nielsen *et al.*, 'Best practice standards for circular RNA research', *Nat Methods*, vol. 19, no. 10, pp. 1208–1220, Oct. 2022, doi: 10.1038/s41592-022-01487-2.

[176] P. J. Cranfill *et al.*, 'Quantitative assessment of fluorescent proteins', *Nat Methods*, vol. 13, no. 7, pp. 557–562, Jul. 2016, doi: 10.1038/nmeth.3891.

[177] D. S. Peabody, 'The RNA binding site of bacteriophage MS2 coat protein.', *EMBO J*, vol. 12, no. 2, pp. 595–600, Feb. 1993, doi: 10.1002/j.1460-2075.1993.tb05691.x.

[178] R. Golmohammadi, K. Valegård, K. Fridborg, and L. Liljas, 'The Refined Structure of Bacteriophage MS2 at 2·8 Å Resolution', *J Mol Biol*, vol. 234, no. 3, pp. 620–639, Dec. 1993, doi: 10.1006/jmbi.1993.1616.

[179] E. Bertrand, P. Chartrand, M. Schaefer, S. M. Shenoy, R. H. Singer, and R. M. Long, 'Localization of ASH1 mRNA Particles in Living Yeast', *Mol Cell*, vol. 2, no. 4, pp. 437–445, Oct. 1998, doi: 10.1016/S1097-2765(00)80143-4.

[180] R. C. L. Olsthoorn, G. Garde, T. Dayhuff, J. F. Atkins, and J. van Duin, 'Nucleotide sequence of a single-stranded RNA phage from Pseudomonas aeruginosa:Kinship to coliphages and conservation of regulatory RNA structures', *Virology*, vol. 206, no. 1, pp. 611–625, Jan. 1995, doi: 10.1016/S0042-6822(95)80078-6.

[181] S. Chattopadhyay, J. Garcia-Mena, J. DeVito, K. Wolska, and A. Das, 'Bipartite function of a small RNA hairpin in transcription antitermination in bacteriophage lambda.', *Proceedings of the National Academy of Sciences*, vol. 92, no. 9, pp. 4061–4065, Apr. 1995, doi: 10.1073/pnas.92.9.4061.

[182] B. Wu *et al.*, 'Synonymous modification results in high-fidelity gene expression of repetitive protein and nucleotide sequences', *Genes Dev*, vol. 29, no. 8, pp. 876–886, Apr. 2015, doi: 10.1101/gad.259358.115.

[183] S. Shao, H. Zhang, Y. Zeng, Y. Li, C. Sun, and Y. Sun, 'TagBiFC technique allows long-term single-molecule tracking of protein-protein interactions in living cells', *Commun Biol*, vol. 4, no. 1, p. 378, Mar. 2021, doi: 10.1038/s42003-021-01896-7.

[184] B. Wu, J. Chen, and R. H. Singer, 'Background free imaging of single mRNAs in live cells using split fluorescent proteins', *Sci Rep*, vol. 4, no. 1, p. 3615, Jan. 2014, doi: 10.1038/srep03615.

[185] S. Y. Park, H. C. Moon, and H. Y. Park, 'Live-cell imaging of single mRNA dynamics using split superfolder green fluorescent proteins with minimal

background', *RNA*, vol. 26, no. 1, pp. 101–109, Jan. 2020, doi: 10.1261/rna.067835.118.
[186] S. Hocine, P. Raymond, D. Zenklusen, J. A. Chao, and R. H. Singer, 'Single-molecule analysis of gene expression using two-color RNA labeling in live yeast', *Nat Methods*, vol. 10, no. 2, pp. 119–121, Feb. 2013, doi: 10.1038/nmeth.2305.
[187] D. Fusco *et al.*, 'Single mRNA Molecules Demonstrate Probabilistic Movement in Living Mammalian Cells', *Current Biology*, vol. 13, no. 2, pp. 161–167, Jan. 2003, doi: 10.1016/S0960-9822(02)01436-7.
[188] J. S. Paige, K. Y. Wu, and S. R. Jaffrey, 'RNA Mimics of Green Fluorescent Protein', *Science (1979)*, vol. 333, no. 6042, pp. 642–646, Jul. 2011, doi: 10.1126/science.1207339.
[189] G. S. Filonov, J. D. Moon, N. Svensen, and S. R. Jaffrey, 'Broccoli: Rapid Selection of an RNA Mimic of Green Fluorescent Protein by Fluorescence-Based Selection and Directed Evolution', *J Am Chem Soc*, vol. 136, no. 46, pp. 16299–16308, Nov. 2014, doi: 10.1021/ja508478x.
[190] A. Autour *et al.*, 'Fluorogenic RNA Mango aptamers for imaging small non-coding RNAs in mammalian cells', *Nat Commun*, vol. 9, no. 1, p. 656, Feb. 2018, doi: 10.1038/s41467-018-02993-8.
[191] E. v. Dolgosheina *et al.*, 'RNA Mango Aptamer-Fluorophore: A Bright, High-Affinity Complex for RNA Labeling and Tracking', *ACS Chem Biol*, vol. 9, no. 10, pp. 2412–2420, Oct. 2014, doi: 10.1021/cb500499x.
[192] S. C. Y. Jeng, H. H. Y. Chan, E. P. Booy, S. A. McKenna, and P. J. Unrau, 'Fluorophore ligand binding and complex stabilization of the RNA Mango and RNA Spinach aptamers', *RNA*, vol. 22, no. 12, pp. 1884–1892, Dec. 2016, doi: 10.1261/rna.056226.116.
[193] A. D. Cawte, P. J. Unrau, and D. S. Rueda, 'Live cell imaging of single RNA molecules with fluorogenic Mango II arrays', *Nat Commun*, vol. 11, no. 1, p. 1283, Mar. 2020, doi: 10.1038/s41467-020-14932-7.
[194] J. U. Guo and D. P. Bartel, 'RNA G-quadruplexes are globally unfolded in eukaryotic cells and depleted in bacteria', *Science (1979)*, vol. 353, no. 6306, pp. aaf5371–aaf5371, Sep. 2016, doi: 10.1126/science.aaf5371.
[195] O. O. Abudayyeh *et al.*, 'C2c2 is a single-component programmable RNA-guided RNA-targeting CRISPR effector', *Science (1979)*, vol. 353, no. 6299, Aug. 2016, doi: 10.1126/science.aaf5573.
[196] L.-Z. Yang *et al.*, 'Dynamic Imaging of RNA in Living Cells by CRISPR-Cas13 Systems', *Mol Cell*, vol. 76, no. 6, pp. 981-997.e7, Dec. 2019, doi: 10.1016/j.molcel.2019.10.024.
[197] Z. Ma, X. Wu, C. J. Krueger, and A. K. Chen, 'Engineering Novel Molecular Beacon Constructs to Study Intracellular RNA Dynamics and Localization', *Genomics Proteomics Bioinformatics*, vol. 15, no. 5, pp. 279–286, Oct. 2017, doi: 10.1016/j.gpb.2017.04.004.
[198] S. Tyagi and F. R. Kramer, 'Molecular Beacons: Probes that Fluoresce upon Hybridization', *Nat Biotechnol*, vol. 14, no. 3, pp. 303–308, Mar. 1996, doi: 10.1038/nbt0396-303.
[199] D. P. Bratu, B.-J. Cha, M. M. Mhlanga, F. R. Kramer, and S. Tyagi, 'Visualizing the distribution and transport of mRNAs in living cells', *Proceedings of the*

National Academy of Sciences, vol. 100, no. 23, pp. 13308–13313, Nov. 2003, doi: 10.1073/pnas.2233244100.

[200] B. Turner-Bridger *et al.*, 'Single-molecule analysis of endogenous β-actin mRNA trafficking reveals a mechanism for compartmentalized mRNA localization in axons', *Proceedings of the National Academy of Sciences*, vol. 115, no. 41, Oct. 2018, doi: 10.1073/pnas.1806189115.

[201] L. S. Kristensen, T. L. H. Okholm, M. T. Venø, and J. Kjems, 'Circular RNAs are abundantly expressed and upregulated during human epidermal stem cell differentiation', *RNA Biol*, vol. 15, no. 2, pp. 280–291, Feb. 2018, doi: 10.1080/15476286.2017.1409931.

[202] J. Rea *et al.*, 'HOTAIRM1 regulates neuronal differentiation by modulating NEUROGENIN 2 and the downstream neurogenic cascade', *Cell Death Dis*, vol. 11, no. 7, p. 527, Jul. 2020, doi: 10.1038/s41419-020-02738-w.

[203] A. Ooi, A. Wong, L. Esau, F. Lemtiri-Chlieh, and C. Gehring, 'A Guide to Transient Expression of Membrane Proteins in HEK-293 Cells for Functional Characterization', *Front Physiol*, vol. 7, Jul. 2016, doi: 10.3389/fphys.2016.00300.

[204] F. M. Wurm, 'Production of recombinant protein therapeutics in cultivated mammalian cells', *Nat Biotechnol*, vol. 22, no. 11, pp. 1393–1398, Nov. 2004, doi: 10.1038/nbt1026.

[205] F. Bollin, V. Dechavanne, and L. Chevalet, 'Design of Experiment in CHO and HEK transient transfection condition optimization', *Protein Expr Purif*, vol. 78, no. 1, pp. 61–68, Jul. 2011, doi: 10.1016/j.pep.2011.02.008.

[206] J.-Y. Tinevez *et al.*, 'TrackMate: An open and extensible platform for single-particle tracking', *Methods*, vol. 115, pp. 80–90, Feb. 2017, doi: 10.1016/j.ymeth.2016.09.016.

[207] D. Ershov *et al.*, 'TrackMate 7: integrating state-of-the-art segmentation algorithms into tracking pipelines', *Nat Methods*, vol. 19, no. 7, pp. 829–832, Jul. 2022, doi: 10.1038/s41592-022-01507-1.

[208] S. P. Shevtsov and M. Dundr, 'Nucleation of nuclear bodies by RNA', *Nat Cell Biol*, vol. 13, no. 2, pp. 167–173, Feb. 2011, doi: 10.1038/ncb2157.

[209] A. Musacchio, 'On the role of phase separation in the biogenesis of membraneless compartments', *EMBO J*, vol. 41, no. 5, Mar. 2022, doi: 10.15252/embj.2021109952.

[210] S. F. Shimobayashi, P. Ronceray, D. W. Sanders, M. P. Haataja, and C. P. Brangwynne, 'Nucleation landscape of biomolecular condensates', *Nature*, vol. 599, no. 7885, pp. 503–506, Nov. 2021, doi: 10.1038/s41586-021-03905-5.

[211] J.-Y. Youn *et al.*, 'Properties of Stress Granule and P-Body Proteomes', *Mol Cell*, vol. 76, no. 2, pp. 286–294, Oct. 2019, doi: 10.1016/j.molcel.2019.09.014.

[212] A. Aulas *et al.*, 'G3BP1 promotes stress-induced RNA granule interactions to preserve polyadenylated mRNA', *Journal of Cell Biology*, vol. 209, no. 1, pp. 73–84, Apr. 2015, doi: 10.1083/jcb.201408092.

[213] Y. Luo, Z. Na, and S. A. Slavoff, 'P-Bodies: Composition, Properties, and Functions', *Biochemistry*, vol. 57, no. 17, pp. 2424–2431, May 2018, doi: 10.1021/acs.biochem.7b01162.

[214] R. Jia, M.-S. Xiao, Z. Li, G. Shan, and C. Huang, 'Defining an evolutionarily conserved role of GW182 in circular RNA degradation', *Cell Discov*, vol. 5, no. 1, p. 45, Sep. 2019, doi: 10.1038/s41421-019-0113-y.

[215] L. Ren *et al.*, 'Mechanisms of circular RNA degradation', *Commun Biol*, vol. 5, no. 1, p. 1355, Dec. 2022, doi: 10.1038/s42003-022-04262-3.

[216] A. Khong, T. Matheny, S. Jain, S. F. Mitchell, J. R. Wheeler, and R. Parker, 'The Stress Granule Transcriptome Reveals Principles of mRNA Accumulation in Stress Granules', *Mol Cell*, vol. 68, no. 4, pp. 808-820.e5, Nov. 2017, doi: 10.1016/j.molcel.2017.10.015.

[217] S. Namkoong, A. Ho, Y. M. Woo, H. Kwak, and J. H. Lee, 'Systematic Characterization of Stress-Induced RNA Granulation', *Mol Cell*, vol. 70, no. 1, pp. 175-187.e8, Apr. 2018, doi: 10.1016/j.molcel.2018.02.025.

[218] R. de Santis, M. G. Garone, F. Pagani, V. de Turris, S. di Angelantonio, and A. Rosa, 'Direct conversion of human pluripotent stem cells into cranial motor neurons using a piggyBac vector', *Stem Cell Res*, vol. 29, pp. 189–196, May 2018, doi: 10.1016/j.scr.2018.04.012.

[219] J. Luo, L. Qu, F. Gao, J. Lin, J. Liu, and A. Lin, 'LncRNAs: Architectural Scaffolds or More Potential Roles in Phase Separation', *Front Genet*, vol. 12, Mar. 2021, doi: 10.3389/fgene.2021.626234.

[220] M. Li, L. Zhao, P. S. Page-McCaw, and W. Chen, 'Zebrafish Genome Engineering Using the CRISPR–Cas9 System', *Trends in Genetics*, vol. 32, no. 12, pp. 815–827, Dec. 2016, doi: 10.1016/j.tig.2016.10.005.

[221] T. J. Kwiatkowski *et al.*, 'Mutations in the *FUS/TLS* Gene on Chromosome 16 Cause Familial Amyotrophic Lateral Sclerosis', *Science (1979)*, vol. 323, no. 5918, pp. 1205–1208, Feb. 2009, doi: 10.1126/science.1166066.

[222] C. Vance *et al.*, 'Mutations in FUS, an RNA Processing Protein, Cause Familial Amyotrophic Lateral Sclerosis Type 6', *Science (1979)*, vol. 323, no. 5918, pp. 1208–1211, Feb. 2009, doi: 10.1126/science.1165942.

[223] J. Lenzi *et al.*, 'ALS mutant FUS proteins are recruited into stress granules in induced Pluripotent Stem Cells (iPSCs) derived motoneurons', *Dis Model Mech*, Jan. 2015, doi: 10.1242/dmm.020099.

[224] R. Insolera, W. Shao, R. Airik, F. Hildebrandt, and S.-H. Shi, 'SDCCAG8 Regulates Pericentriolar Material Recruitment and Neuronal Migration in the Developing Cortex', *Neuron*, vol. 83, no. 4, pp. 805–822, Aug. 2014, doi: 10.1016/j.neuron.2014.06.029.

[225] N. Villa, A. Do, J. W. B. Hershey, and C. S. Fraser, 'Human Eukaryotic Initiation Factor 4G (eIF4G) Protein Binds to eIF3c, -d, and -e to Promote mRNA Recruitment to the Ribosome', *Journal of Biological Chemistry*, vol. 288, no. 46, pp. 32932–32940, Nov. 2013, doi: 10.1074/jbc.M113.517011.

[226] N. Vasan, A. Hutagalung, P. Novick, and K. M. Reinisch, 'Structure of a C-terminal fragment of its Vps53 subunit suggests similarity of Golgi-associated retrograde protein (GARP) complex to a family of tethering complexes', *Proceedings of the National Academy of Sciences*, vol. 107, no. 32, pp. 14176–14181, Aug. 2010, doi: 10.1073/pnas.1009419107.

[227] R. Char and P. Pierre, 'The RUFYs, a Family of Effector Proteins Involved in Intracellular Trafficking and Cytoskeleton Dynamics', *Front Cell Dev Biol*, vol. 8, Aug. 2020, doi: 10.3389/fcell.2020.00779.

[228] W. van Leeuwen, M. VanInsberghe, N. Battich, F. Salmén, A. van Oudenaarden, and C. Rabouille, 'Identification of the stress granule transcriptome via RNA-editing in single cells and in vivo', *Cell Reports Methods*, vol. 2, no. 6, p. 100235, Jun. 2022, doi: 10.1016/j.crmeth.2022.100235.

[229] Y. C. Liao *et al.*, 'RNA Granules Hitchhike on Lysosomes for Long-Distance Transport, Using Annexin A11 as a Molecular Tether', *Cell*, vol. 179, no. 1, pp. 147-164.e20, Sep. 2019, doi: 10.1016/j.cell.2019.08.050.

[230] M. Sunbul *et al.*, 'Super-resolution RNA imaging using a rhodamine-binding aptamer with fast exchange kinetics', *Nat Biotechnol*, vol. 39, no. 6, pp. 686–690, Jun. 2021, doi: 10.1038/s41587-020-00794-3.

[231] Q. Wang *et al.*, 'Inert Pepper aptamer-mediated endogenous mRNA recognition and imaging in living cells', *Nucleic Acids Res*, vol. 50, no. 14, pp. e84–e84, Aug. 2022, doi: 10.1093/nar/gkac368.

[232] J. Martone *et al.*, 'SMaRT lncRNA controls translation of a G-quadruplex-containing mRNA antagonizing the DHX36 helicase', *EMBO Rep*, vol. 21, no. 6, Jun. 2020, doi: 10.15252/embr.201949942.

[233] T. Conrad and U. A. Ørom, 'Cellular Fractionation and Isolation of Chromatin-Associated RNA', 2017, pp. 1–9. doi: 10.1007/978-1-4939-4035-6_1.

[234] K. Jaqaman *et al.*, 'Robust single-particle tracking in live-cell time-lapse sequences', *Nat Methods*, vol. 5, no. 8, pp. 695–702, Aug. 2008, doi: 10.1038/nmeth.1237.

[235] F. Pellegrini *et al.*, 'A KO mouse model for the lncRNA Lhx1os produces motor neuron alterations and locomotor impairment', *iScience*, vol. 26, no. 1, p. 105891, Jan. 2023, doi: 10.1016/j.isci.2022.105891.

9. SCIENTIFIC PRODUCTION

E. D'Ambra *et al.*, 'Circ-Hdgfrp3 shuttles along neurites and is trapped in aggregates formed by ALS-associated mutant FUS', *iScience*, vol. 24, no. 12, p. 103504, Dec. 2021, doi: 10.1016/j.isci.2021.103504. [2]

F. Pellegrini *et al.*, 'A KO mouse model for the lncRNA Lhx1os produces motor neuron alterations and locomotor impairment', *iScience*, vol. 26, no. 1, p. 105891, Jan. 2023, doi: 10.1016/j.isci.2022.105891. [235]